



# 1 Anaerobic oxidation of methane alters sediment records of 2 sulfur, iron and phosphorus in the Black Sea

3 Matthias Egger<sup>1</sup>, Peter Kraal<sup>1</sup>, Tom Jilbert<sup>1,2</sup>, Fatimah Sulu-Gambari<sup>1</sup>, Célia J. Sapart<sup>3,4</sup>, Thomas  
4 Röckmann<sup>3</sup> and Caroline P. Slomp<sup>1</sup>

5 <sup>1</sup>Department of Earth Sciences – Geochemistry, Faculty of Geosciences, Utrecht University, P.O. Box 80021, 3508  
6 TA, Utrecht, The Netherlands

7 <sup>2</sup>Now at: Department of Environmental Sciences, Faculty of Biological and Environmental Sciences, University of  
8 Helsinki, P.O. Box 65 (Viikinkaari 2a), 00014 Helsinki, Finland

9 <sup>3</sup>Institute for Marine and Atmospheric Research Utrecht (IMAU), Utrecht University, Princetonplein 5, 3584 CC  
10 Utrecht, The Netherlands

11 <sup>4</sup>Laboratoire de Glaciologie, Université Libre de Bruxelles, Belgium

12 *Correspondence to:* Matthias Egger (m.j.egger@uu.nl)

13 **Abstract.** The surface sediments in the Black Sea are underlain by extensive deposits of iron (Fe) oxide-rich lake  
14 sediments that were deposited prior to the inflow of marine Mediterranean Sea waters ca. 9000 years ago. The  
15 subsequent downward diffusion of marine sulfate into the methane-bearing lake sediments has led to a multitude of  
16 diagenetic reactions in the sulfate-methane transition zone (SMTZ), including anaerobic oxidation of methane  
17 (AOM) with sulfate. While the sedimentary cycles of sulfur (S), methane and Fe in the SMTZ have been extensively  
18 studied, relatively little is known about the diagenetic alterations of the sediment record occurring below the SMTZ.

19 Here we combine detailed geochemical analyses of the sediment and pore water with multicomponent diagenetic  
20 modeling to study the diagenetic alterations below the SMTZ at two sites in the western Black Sea. We focus on the  
21 dynamics of Fe, S and phosphorus (P) and demonstrate that diagenesis has strongly overprinted the sedimentary  
22 burial records of these elements. Our results show that sulfate-mediated AOM substantially enhances the downward  
23 diffusive flux of sulfide into the deep limnic deposits. During this downward sulfidization, Fe oxides, Fe carbonates  
24 and Fe phosphates (e.g. vivianite) are converted to sulfide phases, leading to an enrichment in solid phase S and the  
25 release of phosphate to the pore water. Below the sulfidization front, high concentrations of dissolved ferrous Fe  
26 ( $\text{Fe}^{2+}$ ) lead to sequestration of downward diffusing phosphate as authigenic vivianite, resulting in a transient  
27 accumulation of total P directly below the sulfidization front.

28 Our model results further demonstrate that downward migrating sulfide becomes partly re-oxidized to sulfate due to  
29 reactions with oxidized Fe minerals, fueling a cryptic S cycle and thus stimulating slow rates of sulfate-driven AOM  
30 ( $\sim 1 - 100 \text{ pmol cm}^{-3} \text{ d}^{-1}$ ) in the sulfate-depleted limnic deposits. However, this process is unlikely to explain the  
31 observed release of dissolved  $\text{Fe}^{2+}$  below the SMTZ. Instead, we suggest that besides organoclastic Fe oxide  
32 reduction, AOM coupled to the reduction of Fe oxides may also provide a possible mechanism for the high  
33 concentrations of  $\text{Fe}^{2+}$  in the pore water at depth. Our results reveal that methane plays a key role in the diagenetic  
34 alterations of Fe, S and P records in Black Sea sediments. The downward sulfidization into the limnic deposits is  
35 enhanced through sulfate-driven AOM with sulfate and AOM with Fe oxides may provide a deep source of dissolved  
36  $\text{Fe}^{2+}$  that drives the sequestration of P in vivianite below the sulfidization front.

37 **1 Introduction**

38 Anaerobic oxidation of methane (AOM), a process initially regarded as a biogeochemical curiosity, functions as an  
39 important sink for oceanic methane (CH<sub>4</sub>) by consuming > 90 % of all CH<sub>4</sub> produced in marine sediments (Knittel  
40 and Boetius, 2009; Reeburgh, 2007). Although recent studies indicate that the biological oxidation of CH<sub>4</sub> could be  
41 coupled to various additional electron acceptors such as nitrate and nitrite (Ettwig et al., 2010; Raghoebarsing et al.,  
42 2006) as well as metal oxides (Beal et al., 2009; Egger et al., 2015b; Riedinger et al., 2014; Scheller et al., 2016;  
43 Segarra et al., 2013; Sivan et al., 2011), sulfate (SO<sub>4</sub><sup>2-</sup>) is commonly thought to be the dominant electron acceptor in  
44 anoxic marine systems (Knittel and Boetius, 2009; Reeburgh, 2007).

45 Nevertheless, a coupling between anaerobic CH<sub>4</sub> oxidation and iron (Fe) oxide reduction (Fe-AOM) could have a  
46 significant impact on sedimentary Fe cycling and related processes such as phosphorus (P) diagenesis, because of the  
47 8:1 Fe-CH<sub>4</sub> stoichiometry of the reaction (Beal et al., 2009; Egger et al., 2015a; Rooze et al., 2016). Environmental  
48 conditions that favor Fe-AOM in marine systems are still poorly understood. The required co-occurrence of pore  
49 water CH<sub>4</sub> and abundant reducible Fe oxides suggests that Fe-AOM may occur in sediments that receive a relatively  
50 high input of Fe oxides compared to the in-situ production of sulfide, which could allow a portion of Fe oxides to  
51 escape the conversion to authigenic Fe sulfides and to remain preserved in the methanogenic sediments below the  
52 zone of SO<sub>4</sub><sup>2-</sup> reduction (Egger et al., 2015b; Riedinger et al., 2014; Rooze et al., 2016). In addition, perturbations  
53 inducing transient diagenesis such as anthropogenic eutrophication or climate change may also create diagenetic  
54 environments that are likely favorable for Fe-AOM, as they provide a mechanism for the burial of Fe oxide-rich  
55 deposits below sulfidic sediment layers (Egger et al., 2015b; Riedinger et al., 2014).

56 The Black Sea represents a good example of a sedimentary system in which transient diagenesis associated with  
57 postglacial sea-level rise has led to the accumulation of sulfidic sediments above Fe oxide-rich deposits. Here, the  
58 establishment of a connection to the Mediterranean Sea through the shallow Bosphorus around 9000 years ago  
59 (Degens and Ross, 1974; Soulet et al., 2011) led to the inflow of marine waters into a freshwater basin, resulting in  
60 permanent salinity/density stratification and in the development of euxinic conditions (i.e. free dissolved sulfide  
61 present in the bottom water), making the current Black Sea the largest permanently anoxic basin on Earth.

62 In the absence of oxygen and metal oxides, SO<sub>4</sub><sup>2-</sup> reduction is the dominant benthic mineralization process of organic  
63 matter in Black Sea surface sediments below the chemocline (~ 100 m depth) (Jørgensen et al., 2001; Thamdrup et  
64 al., 2000). At present, SO<sub>4</sub><sup>2-</sup> penetrates through the modern coccolith ooze (Unit I) and the marine sapropel (Unit II)  
65 sediments and a few meters into the Upper Pleistocene freshwater deposits (Unit III) (Arthur and Dean, 1998;  
66 Degens and Ross, 1974; Jørgensen et al., 2004). Below the SO<sub>4</sub><sup>2-</sup>-bearing zone, methanogenesis takes over as the  
67 dominant process of organic matter degradation, resulting in the buildup of CH<sub>4</sub> in the pore water at depth.

68 Interactions between the cycles of sulfur (S) and CH<sub>4</sub> in Black Sea sediments have been extensively studied during  
69 recent years (Holmkvist et al., 2011b; Jørgensen et al., 2001, 2004; Knab et al., 2009; Leloup et al., 2007) and AOM  
70 coupled to SO<sub>4</sub><sup>2-</sup> reduction (SO<sub>4</sub>-AOM) was found to account for an estimated 7-18 % of total SO<sub>4</sub><sup>2-</sup> reduction in  
71 these sediments (Jørgensen et al., 2001). The production of sulfide in the sulfate-methane transition zone (SMTZ) as  
72 a result of SO<sub>4</sub>-AOM represents the main source of pore water sulfide at depth in the sediment. This intensified  
73 production of sulfide drives an enhanced downward diffusive flux of sulfide into the deep limnic deposits of Unit III,



74 forming a distinct diagenetic sulfidization front recognized as a black band or a series of bands owing to the  
75 conversion of Fe oxides to Fe sulfides (Jørgensen et al., 2004; Neretin et al., 2004).

76 At present, the impact of the downward-migrating sulfidization front on sedimentary P, a key nutrient for marine  
77 phytoplankton, and the potential role of Fe-mediated AOM in the deep limnic deposits remain largely unknown. A  
78 buildup of ferrous Fe ( $\text{Fe}^{2+}$ ) in the pore water at depth as found in previous studies (Holmkvist et al., 2011b;  
79 Jørgensen et al., 2004; Knab et al., 2009), could indicate ongoing Fe reduction in the  $\text{CH}_4$ -bearing deep limnic  
80 sediments and thus a potential coupling between AOM and Fe oxide reduction. The sediment records investigated up  
81 to now, however, do not extend deep enough to allow the sedimentary cycling of Fe and related biogeochemical  
82 processes below the sulfidization front to be investigated. In particular, the presence of abundant dissolved  $\text{Fe}^{2+}$   
83 combined with a potential release of pore water phosphate ( $\text{HPO}_4^{2-}$ ) during reductive dissolution of Fe oxides may be  
84 conducive to the formation of reduced Fe(II)-P minerals such as vivianite ( $\text{Fe}_3(\text{PO})_4 \cdot 8\text{H}_2\text{O}$ ) below the sulfidization  
85 front (Egger et al., 2015a; Hsu et al., 2014; März et al., 2008). Post-depositional diagenetic alterations as a result of  
86 downward sulfidization could therefore overprint burial records of P in the Upper Pleistocene deposits.

87 In this study, we combine detailed geochemical analyses of the sediment and pore water with multicomponent  
88 diagenetic modeling to study the diagenetic alterations below the lake-marine transition at two sites in the western  
89 Black Sea. Focusing on the dynamics of S, Fe and P, we demonstrate that AOM coupled to  $\text{SO}_4^{2-}$  reduction enhances  
90 the downward sulfidization and associated dissolution of Fe oxides, Fe carbonates and vivianite. Below the  
91 sulfidization front, downward diffusing  $\text{HPO}_4^{2-}$  precipitates as vivianite by reaction with the abundant dissolved  $\text{Fe}^{2+}$ .  
92 We propose that organoclastic Fe oxide reduction and/or AOM coupled to the reduction of Fe oxides are the key  
93 processes explaining the high concentrations of dissolved  $\text{Fe}^{2+}$  at depth in the sediment. Trends in total S and P with  
94 depth are significantly altered by the above-mentioned reactions, highlighting that diagenesis may strongly overprint  
95 burial records of these elements below a lake-marine transition.

## 96 2 Materials and methods

### 97 2.1 Sample collection

#### 98 2.1.1 Gravity core sampling

99 Sediment samples were taken at two slope sites in the western Black Sea during a cruise in June 2013 with R/V  
100 Pelagia. Gravity cores containing ~ 7 m of sediment were collected at sites 4 ( $43^\circ 40.6'$  N,  $30^\circ 7.5'$  E; 377 meters  
101 below sea surface (mbss)) and 5 ( $43^\circ 42.6'$  N,  $30^\circ 6.1'$  E; 178 mbss) (Fig. 1), both situated below the current  
102 chemocline (~ 100 m water depth). The core liners were pre-drilled with 2 cm diameter holes in two rows of 10 cm  
103 resolution on opposing sides of the tube, offset by 5 cm and taped prior to coring. Upon recovery, the liners were cut  
104 into 1 m sections, transferred to a temperature-controlled container set at in-situ bottom water temperature ( $11^\circ\text{C}$ )  
105 and secured vertically. Subsequently, the taped holes were cut open and a cut-off syringe was inserted horizontally  
106 directly after opening each hole.

107 From one series of holes, 10 mL of wet sediment was extracted at 20 cm resolution and immediately transferred into  
108 a 65 mL glass bottle filled with saturated NaCl solution for  $\text{CH}_4$  analysis. The NaCl solution was topped up after



109 addition of the sample, ensuring that no air bubbles remained. Each bottle was sealed with a black rubber stopper and  
110 a screw cap and was subsequently stored upside-down at room temperature. From the second series of holes, 20 mL  
111 sediment was extracted at 20 cm resolution, sealed with parafilm that was tightly closed with an elastic band, and  
112 directly inserted into a nitrogen (N<sub>2</sub>)-purged glove box. Subsequently, the sediment was transferred into a 50 mL  
113 centrifuge tube and centrifuged (4500 rpm; 30 min). The supernatant from each centrifuged sample was filtered  
114 through 0.45 μm pore size disposable filters via 20 mL plastic syringes in the glove box and collected in 15 mL  
115 centrifuge tubes. The sediment fraction was stored frozen (-20 °C) for solid phase analysis. Filtered pore water  
116 samples were sub-sampled under N<sub>2</sub> for analysis of dissolved HPO<sub>4</sub><sup>2-</sup>, ammonium (NH<sub>4</sub><sup>+</sup>), dissolved inorganic  
117 carbon (DIC), Fe, manganese (Mn), SO<sub>4</sub><sup>2-</sup> and sulfide (ΣH<sub>2</sub>S = H<sub>2</sub>S + HS<sup>-</sup>) (see section 2.2) Additional samples of 10  
118 mL of sediment were collected at approximately 50 cm resolution and transferred into pre-weighed 15 mL glass vials  
119 to determine porosity from gravimetric water loss.

### 120 2.1.2 Multicore sampling

121 To sample the surface sediment, sediment cores (30-60 cm of sediment and at least 10 cm of overlying water) were  
122 recovered using an octopus multicorer (core diameter 10 cm). After recovery, the cores were stoppered at the base  
123 and at the top and immediately transported to a temperature-controlled container (11 °C). One multicore from each  
124 cast was pre-drilled with 2 cm diameter holes in two rows at 10 cm resolution on opposing sides of the tube, offset  
125 by 5 cm, and taped prior to coring. These holes were sampled for CH<sub>4</sub> as described for the gravity cores. Another  
126 core was directly inserted into a N<sub>2</sub>-purged glove box through an airtight hole in the base. A bottom water sample  
127 was collected using a 20 mL plastic syringe and the remaining bottom water was removed with a Tygon tube.  
128 Subsequently, the core was sliced anoxically with decreasing resolution at depth, i.e. 0.5 cm resolution for the first 0-  
129 2 cm, 1 cm resolution between 2-10 cm, 2 cm resolution between 10-20 cm and 4 cm resolution for the rest of the  
130 core (> 20 cm). For each slice a sub-sample was placed in a pre-weighed 15 mL glass vial for water content and solid  
131 phase analysis and stored under N<sub>2</sub> in airtight jars at -20 °C. A second sub-sample was transferred to a 50 mL  
132 centrifuge tube and centrifuged (4500 rpm; 30 min). Both the supernatant water from each centrifuged sample and  
133 the bottom water sample were subsequently processed as described for the gravity cores.

134 Visual alignment of the pore water profiles from the multicores with those of the gravity cores showed that the first ~  
135 20 to 30 cm of sediment was lost during long coring. At site 5, the sediment in the multicore consisted of a gray and  
136 homogeneous turbidite below 1.5 cm depth. The depth for the gravity core at site 5 was thus corrected for the loss of  
137 the marine deposits, which were previously reported to be about 50 cm thick at a site in close proximity to site 5  
138 (43°42.63' N, 30°6.12' E; 181 mbss) (Jørgensen et al., 2004)

### 139 2.2 Pore water subsampling

140 A sub-sample of 0.5 mL was immediately transferred into a glass vial containing 1.5 mL of 8 M NaOH solution for  
141 analysis of dissolved sulfide. Sub-samples for total dissolved Fe and Mn, which are assumed to represent Fe(II) and  
142 Mn(II), were acidified with 10 μL 35 % suprapur HCl per mL of sub-sample. Another 1 mL of pore water for HPO<sub>4</sub><sup>2-</sup>  
143 analysis was acidified with 4 μL 5 M HCl. Pore water SO<sub>4</sub><sup>2-</sup> was analyzed with ion chromatography (IC) in a 10-fold



144 diluted sample (0.15 mL of pore water with 1.35 mL of de-oxygenated UHQ water). Sub-samples for DIC analysis  
145 (0.5 mL) were collected in glass vials (4.9 mL) to which 4.4 mL of 25 g/L NaCl solution was added, making sure  
146 that no headspace remained. Aliquots of the remaining pore water were used for the measurement of alkalinity  
147 (determined onboard by titrating 1 mL of untreated sub-sample with 0.01 M HCl; results presented in the  
148 Supplementary Information only) and  $\text{NH}_4^+$ . All sub-samples were stored at 4 °C and brought to room temperature  
149 just before analysis. Subsampling for sulfide was performed immediately after filtration and all other subsampling  
150 was performed within 4 hours of core recovery.

151 Pore water sub-samples for sulfide,  $\text{HPO}_4^{2-}$  and DIC were directly analyzed onboard using an auto analyzer. Sub-  
152 samples for dissolved Fe and Mn were analyzed onshore by ICP-OES (Perkin Elmer Optima 3000 Inductively  
153 Coupled Plasma - Optimal Emission Spectroscopy). For the analysis of pore water  $\text{CH}_4$ , a volume of 10 mL  $\text{N}_2$  was  
154 injected into the  $\text{CH}_4$  serum flasks (while a needle inserted through the septum allowed 10 mL of water to escape) to  
155 create a headspace from which a subsample was collected with a gas-tight syringe. Subsequently,  $\text{CH}_4$  concentrations  
156 were determined in the home laboratory after injection into a Thermo Finnigan Trace GC gas chromatograph (Flame  
157 Ionization Detector).  $\delta^{13}\text{C-CH}_4$  and  $\delta\text{D-CH}_4$  (D, deuterium) were analyzed by Continuous Flow Isotope Ratio Mass  
158 Spectrometry (CF-IRMS) as described in detail in (Brass and Röckmann, 2010) and (Sapart et al., 2011).

### 159 **2.3 Bulk sediment analysis**

160 Sediment samples were freeze-dried, powdered and ground in an agate mortar in an argon (Ar)-filled glove box and  
161 split into oxic and anoxic fractions. Samples from the oxic fraction were used for total elemental and organic carbon  
162 ( $\text{C}_{\text{org}}$ ) analyses under normal atmospheric conditions, whereas anoxic splits for sediment P and Fe speciation were  
163 kept under an inert, oxygen-free Ar or  $\text{N}_2$  atmosphere at all times to avoid oxidation artefacts (Kraal and Slomp,  
164 2014; Kraal et al., 2009).

#### 165 **2.3.1 Total elemental composition and organic carbon**

166 A split of ~ 125 mg of freeze-dried sediment was dissolved overnight in 2.5 mL HF (40 %) and 2.5 mL of  
167  $\text{HClO}_4/\text{HNO}_3$  mixture, in a closed Teflon bomb at 90 °C. The acids were then evaporated at 160 °C and the resulting  
168 gel was dissolved overnight in 1 M  $\text{HNO}_3$  at 90 °C. Total elemental concentrations in the 1 M  $\text{HNO}_3$  solutions were  
169 determined by ICP-OES. A second split of 0.3 g freeze-dried sediment was used to determine the  $\text{C}_{\text{org}}$  content using  
170 an elemental analyzer (Fison Instruments model NA 1500 NCS) after carbonate removal from the sediment with two  
171 washes with 1 M HCl (4 h and 12 h) followed by two washes with UHQ water and subsequent drying of the samples  
172 (Van Santvoort et al., 2002).

#### 173 **2.3.2 Sediment P fractionation**

174 To determine the solid phase partitioning of P, aliquots of 0.1 g dried sediment were subjected to the SEDEX  
175 sequential extraction procedure after Ruttenberg (1992), as modified by Slomp et al. (1996b), but including the first  
176  $\text{MgCl}_2$  step (Table 1). Sediment P was fractionated as follows: i) exchangeable-P (“ $\text{P}_{\text{exch}}$ ”, extracted by 1 M  $\text{MgCl}_2$ ,  
177 pH 8, 0.5 h), ii) Fe-associated P (“ $\text{P}_{\text{Fe}}$ ”, extracted by citrate-bicarbonate-dithionite (CDB), buffered to pH 7.5 with Na



178 citrate/Na bicarbonate, 8 h, followed by 1 M MgCl<sub>2</sub>, pH 8, 0.5 h), iii) authigenic Ca-P (“P<sub>authi Ca-P</sub>”, including  
179 carbonate fluorapatite, biogenic hydroxyapatite and CaCO<sub>3</sub>-bound P, extracted by 1 M Na acetate solution, buffered  
180 to pH 4 with acetic acid, 6 h, followed by 1 M MgCl<sub>2</sub>, pH 8, 0.5 h), iv) detrital Ca-P (“P<sub>detr</sub>”, extracted by 1 M HCl,  
181 24 h) and v) organic P (“P<sub>org</sub>”, after ashing at 550 °C for 2 h, extracted by 1 M HCl, 24 h). The MgCl<sub>2</sub> washes in  
182 steps ii and iii were to ensure that any HPO<sub>4</sub><sup>2-</sup> re-adsorbed during CDB or acetate extraction was removed and  
183 included in the pools of Fe-associated P and authigenic Ca-P, respectively. Sediments were shielded from oxygen  
184 inside an Ar-filled glovebox until step 3 of the SEDEX procedure to eliminate the potential conversion of Ca-P to  
185 Fe-bound P due to pyrite oxidation upon oxygen exposure (Kraal and Slomp, 2014; Kraal et al., 2009). Dissolved  
186 HPO<sub>4</sub><sup>2-</sup> in the CDB solution was analyzed by ICP-OES. For all other solutions, HPO<sub>4</sub><sup>2-</sup> was determined  
187 colorimetrically (Strickland and Parsons, 1972) on a Shimadzu spectrophotometer using the ammonium  
188 heptamolybdate – ascorbic acid method.

### 189 2.3.3 Sediment Fe fractionation

190 Sediment Fe was fractionated into i) carbonate associated Fe (“Fe<sub>carb</sub>”, including siderite and ankerite, extracted by 1  
191 M Na-acetate brought to pH 4.5 with acetic acid, 24 h), ii) easily reducible (amorphous) oxides (“Fe<sub>ox1</sub>”, including  
192 ferrihydrite and lepidocrocite, extracted by 1 M hydroxylamine-HCl, 24 h), iii) reducible (crystalline) oxides  
193 (“Fe<sub>ox2</sub>”, including goethite, hematite and akagenéite, extracted by Na-dithionite buffer, pH 4.8, 2 h) and iv) Fe in  
194 recalcitrant oxides (mostly magnetite, “Fe<sub>mag</sub>”, extracted by 0.2 M ammonium oxalate / 0.17 M oxalic acid solution,  
195 2 h), according to Poulton and Canfield (2005), using a 50 mg aliquot of dried sediment (Table 1). An additional  
196 aliquot of 50 mg was subjected to an adapted sequential extraction procedure after Claff et al. (2010), separating  
197 labile Fe(II) (“Fe(II)<sub>HCl</sub>”) and Fe(III) (“Fe(III)<sub>HCl</sub>”) using 1 M HCl (4 h) from crystalline Fe oxide minerals  
198 (“Fe(II)<sub>CDB</sub>”, Na-dithionite buffer, pH 4.8, 4 h) and from pyrite (“Fe<sub>pyrite</sub>”, concentrated nitric acid, 2 h), for all  
199 multicores as well as for the long core at site 4 (Table 1).

200 At site 4 (multicore only) and 5 (multicore and gravity core), aliquots of 0.5 g dried sediment were used to  
201 sequentially determine the amount of FeS (acid volatile sulfur, “AVS”, using 6 M HCl) and FeS<sub>2</sub> (chromium  
202 reducible sulfur, “CRS”, using acidic chromous chloride solution) via the passive diffusion method described by  
203 (Burton et al., 2008) using iodometric titration of the ZnS formed in the alkaline Zn acetate traps to quantify AVS  
204 and CRS (Table 1).

## 205 2.4 Diagenetic model

### 206 2.4.1 General form

207 A multicomponent transient diagenetic model was developed for site 4 based on existing diagenetic models (Reed et  
208 al., 2011a, 2011b; Rooze et al., 2016) to gain a better understanding of the transient diagenesis in Black Sea  
209 sediments and to investigate the potential for Fe-AOM as a source of pore water Fe<sup>2+</sup> at depth. The model describes  
210 the cycling of dissolved and particulate chemical species in a 1D sediment column (Berner, 1980) and its domain is  
211 represented by 2000 grid cells that capture the upper 2000 cm of the sediment (i.e. vertical resolution of 1 cm). A  
212 total of 25 different chemical species (Table 2) were subjected to a suite of biogeochemical reactions (Table 3) and



213 vertical transport through burial, as well as molecular diffusion for dissolved species (Boudreau, 1997; Soetaert et  
 214 al., 1996; Wang and Van Cappellen, 1996). The general diagenetic equations for solid (Eq. (1)) and dissolved species  
 215 (Eq. (2)) are, respectively,

$$216 \quad (1 - \phi) \frac{\partial C_S}{\partial t} = (1 - \phi)v \frac{\partial C_S}{\partial x} + \sum R_S \quad (1)$$

$$217 \quad \phi \frac{\partial C_{aq}}{\partial t} = \phi D' \frac{\partial^2 C_{aq}}{\partial x^2} - \phi u \frac{\partial C_{aq}}{\partial x} + \sum R_{aq} \quad (2)$$

218 where  $C_S$  is the concentration of the solid species ( $\text{mol L}^{-1}$ ; mass per unit volume of solids),  $C_{aq}$  the concentration of  
 219 the dissolved species ( $\text{mol L}^{-1}$ ; mass per unit volume of pore water),  $t$  is time (yr),  $\phi$  the sediment porosity,  $x$  the  
 220 distance from the sediment-water interface (cm),  $D'$  the diffusion coefficients of dissolved species in the sediment  
 221 ( $\text{cm}^2 \text{ yr}^{-1}$ ) adjusted for the considered setting (Supplementary Table S1) (Boudreau, 1997) and corrected for the  
 222 tortuosity in the porous medium (Boudreau, 1996) (see Supplementary Information).  $\sum R_S$  and  $\sum R_{aq}$  are the net  
 223 reaction rates of the solid and dissolved species from the chemical reactions they participate in (Table 3), and  $v$  and  
 224  $u$  the advective velocities ( $\text{cm yr}^{-1}$ ) of the solid and the dissolved species, respectively. Porosity and advective  
 225 velocities were described by depth-dependent functions to account for sediment compaction (Meysman et al., 2005;  
 226 Reed et al., 2011a) (see Supplementary Information and Supplementary Fig. S1).

227 Reactions considered by the model and corresponding reaction equations are given in Tables 3 and 4, respectively,  
 228 and are divided into primary redox reactions and other biogeochemical reactions, including various mineral  
 229 formation and dissolution reactions (Reed et al., 2011a, 2011b; Rooze et al., 2016). Corresponding reaction  
 230 parameters were mostly taken from the literature or, if these were not available or no fit to the data could be obtained  
 231 with existing parameter ranges, constrained using the extensive geochemical dataset for site 4 (Table 5). To account  
 232 for differences in reactivity and crystallinity between different species, organic matter and Fe oxides are divided into  
 233 three different pools, representing highly reactive ( $\alpha$ ), less reactive ( $\beta$ ) and non-reactive (i.e. inert) ( $\gamma$ ) phases. For the  
 234 Fe oxides, only the  $\alpha$  phase is used by organoclastic Fe reduction (Table 3), while both the  $\alpha$  and  $\beta$  phase are used by  
 235 Fe-AOM (Rooze et al., 2016).

236 The succession of oxidants during organic matter decomposition (Froelich et al., 1979) is described by means of  
 237 Monod kinetics (Table 4), inhibiting degradation pathways in the presence of oxidants with higher metabolic free  
 238 energy yields and switching off pathways when an oxidant is exhausted (Berg et al., 2003; Boudreau, 1996; Reed et  
 239 al., 2011b; Rooze et al., 2016; Wang and Van Cappellen, 1996). Corresponding limiting concentrations for the  
 240 oxidants are taken from (Reed et al., 2011a) (Table 5). In addition, an attenuation factor,  $\Psi$ , is used to slow down  
 241 organic matter degradation through  $\text{SO}_4^{2-}$  reduction and methanogenesis, thus allowing for better preservation of  
 242 organic matter under anoxic bottom water conditions (Moodley et al., 2005; Reed et al., 2011a, 2011b).

243 Cycling of S is simulated using five different chemical species, i.e. Fe monosulfides (FeS), pyrite ( $\text{FeS}_2$ ), elemental S  
 244 ( $\text{S}_0$ ), dissolved sulfide and pore water  $\text{SO}_4^{2-}$  (Table 2), combined in a network of various biogeochemical reactions  
 245 (Table 3). The  $\text{CH}_4$  cycle includes  $\text{CH}_4$  production from organic matter and from  $\text{CO}_2$ , as well as  $\text{CH}_4$  oxidation  
 246 coupled to the reduction of  $\text{O}_2$ ,  $\text{SO}_4^{2-}$  and  $\text{Fe}(\text{OH})_3$  (Table 3). Although Mn-oxides have also been suggested to be a  
 247 thermodynamically favorable electron acceptor for AOM (Beal et al., 2009), they were not included in the model  
 248 because of the relatively low Mn concentrations ( $\sim 15 \mu\text{mol g}^{-1}$  for total sedimentary Mn and  $< 30 \mu\text{M}$  for dissolved



249  $\text{Mn}^{2+}$ ; Supplementary Fig. S2 and S3) when compared to Fe and the likely presence of most of the Mn in the form of  
250 Mn-carbonates.

251 The P forms included in the model are pore water  $\text{HPO}_4^{2-}$ , authigenic Ca-P, organic P and detrital P, as well as Fe-  
252 bound P, i.e. P associated with Fe oxides and P in vivianite (Table 2). The removal of dissolved  $\text{Fe}^{2+}$  through  
253 formation of the Fe minerals FeS, siderite ( $\text{FeCO}_3$ ) and vivianite is also included in the model (Table 3).

254 The boundary conditions at the sediment surface were specified as time-dependent depositional fluxes for the  
255 particulate components and as fixed bottom water concentrations for the dissolved species, while a zero gradient  
256 boundary condition was set for all chemical species at the base of the model domain (Fig. 2 and Supplementary  
257 Table S2). To avoid potential interferences of the lower boundary conditions with the model results in the upper  
258 sediments, the model depth was set to 2000 cm (see Supplementary Fig. S4). In this paper, only the upper 800 cm are  
259 shown. However, all profiles extending over the full depth range are provided in the Supplementary Information file  
260 (Supplementary Fig. S3 and Fig. S5). The model code was written in R using the marelac geochemical dataset  
261 package (Soetaert et al., 2010) and the ReacTran package (Soetaert and Meysman, 2012) to calculate the transport in  
262 porous media. The set of ordinary differential equations was subsequently solved numerically with the Isoda  
263 integrator algorithm (Hindmarsh, 1983; Petzoldt, 1983)

#### 264 **2.4.2 Transient scenario**

265 The model applied in this study simulates the sediment deposition during the last 25000 years. A constant mass  
266 accumulation rate of  $0.06 \text{ g cm}^{-2} \text{ yr}^{-1}$  over the Holocene was assumed. In order to reduce the computing time for the  
267 freshwater period, a higher mass accumulation rate of  $1 \text{ g cm}^{-2} \text{ yr}^{-1}$  was used between 25000 and 10000 years before  
268 present (B.P.) and all fluxes were corrected accordingly (i.e. multiplied with a factor of 16.67). The best fit to the  
269 chloride ( $\text{Cl}^-$ ) profile, which can be used to estimate the timing of the Mediterranean saltwater inflow into the Black  
270 Sea basin, was obtained assuming an initial salinity of 1 for the freshwater lake and a linear increase to a salinity of  
271 22 starting around 9000 years ago (Fig. 2). Such a salinization scenario compares well to a previous salinity  
272 reconstruction by Soulet et al. (2010). However, a constant salinity over the last 2000 years, as suggested by these  
273 authors, resulted in a pore water gradient that was too shallow when compared to the measured pore water  $\text{Cl}^-$  profile  
274 (Supplementary Fig. S4). Therefore, the period with constant salinity of 22 was adjusted to 100 years to fit the data.

275 A shift from oxic towards euxinic conditions around 7600 years B.P., with a peak in organic matter loading around  
276 5300 years B.P. and constant elevated organic matter fluxes after 2700 years B.P. was assumed, following a recent  
277 study comprising data from seven sediment cores collected from the Black Sea (Eckert et al., 2013) (Fig. 2). In  
278 addition, the input of organic matter was assumed to increase again in the last century, reflecting anthropogenic  
279 eutrophication of waters on the adjacent continental shelf as previously reported (Capet et al., 2013; Kemp et al.,  
280 2009). With the development of anoxic and sulfidic bottom-water conditions, depositional fluxes of reactive Fe  
281 oxides were assumed to be zero (Fig. 2). In contrast, fluxes of Fe sulfides are high under euxinic conditions and  
282 dominated by  $\text{FeS}_2$ .





## 283 3 Results

### 284 3.1 Pore water profiles

285 Pore water profiles of  $\text{SO}_4^{2-}$  show a linear decrease from  $\sim 17$  mM at the sediment water interface to a depth of  $\sim 230$   
286 cm at both sites, below which  $\text{CH}_4$  starts to accumulate in the pore water (Fig. 3). Bubble formation and degassing of  
287  $\text{CH}_4$  during gravity coring could not be avoided because of the high concentrations of  $\text{CH}_4$  in the limnic deposits  
288 (above the saturation of ca 1.3 mM  $\text{CH}_4$  at atmospheric pressure; (Jørgensen et al., 2001; Yamamoto et al., 1976)).  
289 Higher concentrations measured at site 5 are indicative of less  $\text{CH}_4$  degassing. Observations of increased bubble  
290 formation with depth during coring suggest that decreasing  $\text{CH}_4$  concentrations below 300 cm reflect enhanced  
291 outgassing with increasing levels of  $\text{CH}_4$  in the deeper sediments. Pore water profiles of  $\text{NH}_4^+$  at both sites are  
292 similar and concentrations increase to  $\sim 3$  mM at depth, suggesting that actual  $\text{CH}_4$  concentrations at both sites could  
293 be comparable. Most of the  $\text{CH}_4$  values thus only indicate the presence or absence of  $\text{CH}_4$  and thus are not a  
294 quantitative measure. Modeled pore water concentrations of  $\text{CH}_4$  on the other hand, show a steep increase below the  
295 SMTZ, comparable to the gradient observed at site 5, and build up to concentrations of  $\sim 20$  mM at depth  
296 (Supplementary Fig. S3).

297 The removal of both  $\text{SO}_4^{2-}$  and  $\text{CH}_4$  around 230 cm depth marks the SMTZ, where  $\text{SO}_4$ -AOM drives the production  
298 of dissolved sulfide, DIC and alkalinity (Supplementary Fig. S3) and diffusion of these pore water constituents away  
299 from the SMTZ (Fig. 3). Below the sulfide diffusion front,  $\text{Fe}^{2+}$  accumulates in the pore water. Dissolved  $\text{HPO}_4^{2-}$   
300 reaches a maximum around the depth where sulfide levels drop below the detection limit of  $1 \mu\text{mol L}^{-1}$ , followed by  
301 a steep decrease with depth. Concentrations of pore water  $\text{Mn}^{2+}$  are more than an order of magnitude lower than  
302 those of dissolved  $\text{Fe}^{2+}$ , and decrease from the sediment surface until  $\sim 200$  cm depth, below which they slightly  
303 increase again (Supplementary Fig. S3).

304 The isotopic composition of pore water  $\text{CH}_4$  (available for site 5 only) seems not affected by the  $\text{CH}_4$  loss and reveals  
305 a biological origin in the limnic deposits, with hydrogenotrophic carbonate reduction, i.e. microbial reduction of  $\text{CO}_2$   
306 to  $\text{CH}_4$  as the main methanogenic pathway for the range of  $\text{CH}_4$  isotope ratios observed in these sediments (Fig. 4)  
307 (Whiticar, 1999). Upward diffusing  $\text{CH}_4$  shows a gradual depletion in  $\delta^{13}\text{C-CH}_4$  from  $\sim -74$  ‰ at depth to  $\sim -96$  ‰  
308 around the SMTZ, followed by subsequent progressive  $^{13}\text{C}$  enrichment towards the sediment surface.  $\delta\text{D-CH}_4$  shows  
309 a small enrichment from  $-226$  ‰ at depth to  $\sim -208$  ‰ at the SMTZ and a strong shift towards high  $\delta\text{D-CH}_4$  values of  
310 up to  $\sim 113$  ‰.

### 311 3.2 Solid phase profiles

312 A pronounced excursion in sedimentary  $\text{C}_{\text{org}}$  at site 4 in combination with a shift from gray clay deposits to micro-  
313 laminated black sediments indicates that the lake-marine transition, i.e. the transition between the marine sapropel  
314 Unit II and the deep limnic sediments of Unit III (Arthur and Dean, 1998; Degens and Ross, 1974), is located around  
315 a sediment depth of  $\sim 90$  cm at site 4 (Fig. 5). At site 5, Unit I and Unit II were lost due to a turbidite, explaining the  
316 low concentrations of  $\text{C}_{\text{org}}$  in the upper sediments.

317 Concentrations of solid S increase with decreasing depth from  $20 \mu\text{mol g}^{-1}$  below 300 cm (sulfidization front) to  $\sim$   
318  $400 \mu\text{mol g}^{-1}$  in the upper 100 cm at both sites and are dominated by  $\text{FeS}_2$  (Fig. 5). Iron oxides show a decrease from



319  $\sim 100 \mu\text{mol g}^{-1}$  at depth to  $\sim 50 \mu\text{mol g}^{-1}$  in the sediments between 100 – 300 cm and a further decrease to  $\sim 10 \mu\text{mol}$   
320  $\text{g}^{-1}$  closer to the sediment surface. Amorphous Fe oxides ( $\text{Fe}_{\text{ox1}}$ ) and more crystalline oxides ( $\text{Fe}_{\text{ox2}}$ ) both account for  
321 half the total amount of Fe oxides, with a small contribution of recalcitrant oxides ( $\text{Fe}_{\text{mag}}$ ) (Supplementary Fig. S2).  
322 The results from the two different Fe extractions applied in this study (Table 1) generally compare well  
323 (Supplementary Fig. S2). Note, however, that the Fe oxides in Fig. 5 represent the results from the extraction after  
324 Poulton and Canfield (2005). Results from the Fe extractions modified from Claff et al. (2010) are provided in the  
325 Supplementary Information only. Sedimentary Mn content is relatively low at all three sites, ranging from  $\sim 5$ -10  
326  $\mu\text{mol g}^{-1}$  in the marine sediments to  $\sim 15 \mu\text{mol g}^{-1}$  in the deep limnic deposits of Unit III (Supplementary Fig. S2).  
327 Sediments below the sulfidization front are characterized by high Fe carbonate contents of  $\sim 100 \mu\text{mol g}^{-1}$ . The sharp  
328 depletion in Fe carbonate around the sulfidization front could only be reproduced in the model by assuming Fe  
329 carbonate dissolution by dissolved sulfide (Table 3). These results suggest a conversion of reactive Fe from  
330 carbonate toward sulfide phases in the presence of abundant dissolved sulfide.

331 Units I and II show high concentrations of organic P, which accounts for  $\sim 30 \%$  of total P in these sediments (Fig.  
332 5). Low organic P and high concentrations of detrital P in the upper sediments at site 5 are due to the turbidite. The  
333 limnic deposits of Unit III are generally depleted in organic P ( $< 6 \%$  of total P) and enriched in detrital P.  
334 Authigenic Ca-P shows little variation in the sediments of Unit III, accounting for  $\sim 20$  to  $30 \%$  of total P at the two  
335 sites. The contribution of Fe-associated P, on the other hand, is reduced in the limnic deposits of Unit III exposed to  
336 the downward diffusing sulfide ( $\sim 20 \%$ ) when compared to the sediments below the sulfidization front ( $\sim 30 \%$ ).  
337 Concentrations of exchangeable P are  $< 2 \mu\text{mol g}^{-1}$  for sediments above the SMTZ and  $< 1 \mu\text{mol g}^{-1}$  for sediments at  
338 depth (data not shown).

339 Modeled  $\text{SO}_4^{2-}$  reduction rates show two distinct peaks of  $\sim 2 \text{nmol cm}^{-3} \text{d}^{-1}$  in the sediments of Unit I and II, as well  
340 as an additional peak in the sediments around the SMTZ (Fig. 6). Rates of methanogenesis are highest in the organic-  
341 rich marine deposits ( $\sim 0.2 - 0.3 \text{nmol cm}^{-3} \text{d}^{-1}$ ) and generally around  $\sim 50 \text{pmol cm}^{-3} \text{d}^{-1}$  in the limnic deposits. The  
342 sediments around the SMTZ are further characterized by high rates of  $\text{SO}_4$ -AOM ( $\sim 0.3 \text{nmol cm}^{-3} \text{d}^{-1}$ ), whereas  
343 sediments directly below the sulfidization front show enhanced rates of  $\text{S}_0$  disproportionation ( $\sim 60 \text{pmol cm}^{-3} \text{d}^{-1}$ ).  
344 Organoclastic  $\text{SO}_4^{2-}$  reduction provides the main source for pore water sulfide in the organic-rich marine deposits,  
345 while  $\text{SO}_4$ -AOM and  $\text{S}_0$  disproportionation are the dominant sources of dissolved sulfide in sediments around the  
346 SMTZ and directly below the sulfidization front, respectively. Rates of Fe-AOM are generally low ( $\sim 0.1 \text{pmol cm}^{-3}$   
347  $\text{d}^{-1}$ ) and restricted to the limnic deposits only.

348 The temporal evolution in pore water and solid phase constituents illustrates the impact of the lake-marine transition  
349 on the sediment geochemistry (Fig. 7). Concentrations of pore water  $\text{Cl}^-$  and  $\text{SO}_4^{2-}$  increase with the intrusion of  
350 marine Mediterranean Sea waters ca. 9000 years ago, accompanied by a decrease in dissolved  $\text{CH}_4$  and accumulation  
351 of pore water sulfide in the shallower sediments. Dissolved  $\text{Fe}^{2+}$  becomes restricted to non-sulfidic pore waters at  
352 depth, while  $\text{HPO}_4^{2-}$  and solid S start to accumulate in the presence of dissolved sulfide. Iron oxides decrease in the  
353 surface sediments as well as in the sediments at depth. Vivianite, on the other hand, becomes increasingly enriched in  
354 sediments below the downward diffusing sulfide front.

355 **4. Discussion**356 **4.1 Coupled S, CH<sub>4</sub> and Fe dynamics**357 **4.1.1 Organoclastic SO<sub>4</sub><sup>2-</sup> reduction**

358 Model-derived areal rates of SO<sub>4</sub><sup>2-</sup> reduction of ~ 0.72 mmol m<sup>-2</sup> d<sup>-1</sup> (Table 6), i.e. the total amount of SO<sub>4</sub><sup>2-</sup> reduced  
359 per square meter of sea floor, are in good agreement with previous estimates of 0.65-1.43 mmol m<sup>-2</sup> d<sup>-1</sup> for sediments  
360 of the Black Sea (Jørgensen et al., 2001). SO<sub>4</sub><sup>2-</sup> reduction accounts for > 90 % of total organic matter degradation in  
361 the model (Table 6), supporting previous conclusions that SO<sub>4</sub><sup>2-</sup> reduction represents the dominant mineralization  
362 process of organic matter in sediments below the chemocline (Jørgensen et al., 2001; Thamdrup et al., 2000).

363 The depth-dependent rate profile of SO<sub>4</sub><sup>2-</sup> reduction shows two distinct peaks of ~ 2 nmol cm<sup>-3</sup> d<sup>-1</sup> associated with  
364 organoclastic SO<sub>4</sub><sup>2-</sup> reduction in the organic matter rich marine deposits of Unit I and Unit II. These high rates  
365 compare well with literature values of 0.1 - 20 nmol cm<sup>-3</sup> d<sup>-1</sup> (Holmkvist et al., 2011b; Jørgensen et al., 2001, 2004;  
366 Knab et al., 2009; Leloup et al., 2007). Thus, like previous modeling approaches based on hybrid modeling with  
367 experimentally measured SO<sub>4</sub><sup>2-</sup> reduction rates (SRR) in the uppermost sediment layers (Jørgensen et al., 2001), the  
368 transient diagenetic model developed in this study is capable of reproducing the high rates of SO<sub>4</sub><sup>2-</sup> reduction near the  
369 sediment surface. Our model further demonstrates that the two SRR peaks in the sediments of Unit I and Unit II are  
370 not reflected in the pore water profile of SO<sub>4</sub><sup>2-</sup>, indicating that SRR estimates based on pore water profiles of SO<sub>4</sub><sup>2-</sup>  
371 alone may underestimate the actual rate of SO<sub>4</sub><sup>2-</sup> reduction in marine sediments.

372 **4.1.2 SO<sub>4</sub>-AOM**

373 Pore water profiles of SO<sub>4</sub><sup>2-</sup>, CH<sub>4</sub>, sulfide and DIC reveal a distinct SMTZ around 230 cm depth at both sites, where  
374 SO<sub>4</sub>-AOM with upward diffusing CH<sub>4</sub> results in the concomitant removal of pore water SO<sub>4</sub><sup>2-</sup> and CH<sub>4</sub> and in the  
375 accumulation of dissolved sulfide and DIC in the pore waters of these sediments (Fig. 3). The depth of the SMTZ  
376 and the steep increase in CH<sub>4</sub> to > 3 mM below the SMTZ found in this study are consistent with earlier observations  
377 in sediments of the western Black Sea (Holmkvist et al., 2011b; Jørgensen et al., 2001, 2004; Knab et al., 2009;  
378 Leloup et al., 2007). The location of the SMTZ, however, has progressed downwards in the last 9000 years,  
379 following the inflow of SO<sub>4</sub><sup>2-</sup>-rich salt water into the Black Sea basin (Fig. 7).

380 In the model, SO<sub>4</sub>-AOM results in enhanced rates of SO<sub>4</sub><sup>2-</sup> reduction at the SMTZ of ~ 0.3 nmol cm<sup>-3</sup> d<sup>-1</sup> (Fig. 8).  
381 Calculated areal rates of SO<sub>4</sub>-AOM of ~ 0.17 mmol m<sup>-2</sup> d<sup>-1</sup> suggest that AOM accounts for ~ 19 % of the total SO<sub>4</sub><sup>2-</sup>  
382 reduction in these sediments (Table 6). Such a high contribution of AOM is close to the range of previous estimates  
383 of 7-18 % (Jørgensen et al., 2001, 2004). Around the SMTZ, SO<sub>4</sub>-AOM is responsible for ~ 90 % of the total SO<sub>4</sub><sup>2-</sup>  
384 reduction (Fig. 6 and Table 6), thus enhancing the downward diffusive flux of sulfide into the deep limnic deposits of  
385 Unit III. Our model suggests that without this additional source of sulfide through SO<sub>4</sub>-AOM, the sulfidization front  
386 would currently be located around 150 cm depth in the sediment (Fig. 8).

387 The consumption of upward diffusing CH<sub>4</sub> by SO<sub>4</sub><sup>2-</sup>-driven AOM leads to a progressive enrichment of <sup>13</sup>C and D in  
388 the residual CH<sub>4</sub> above the SMTZ (Fig. 4) due to the preferential oxidation of isotopically light CH<sub>4</sub> during SO<sub>4</sub>-  
389 AOM (Alperin et al., 1988; Martens et al., 1999; Whiticar, 1999). Modeled concentrations of CH<sub>4</sub> indicate that the



390 measurements above the sulfidization front at site 5 are likely less affected by outgassing during core recovery (Fig.  
391 4) and can thus be used to derive kinetic isotope fractionation factors for carbon ( $\epsilon_C$ ) and hydrogen ( $\epsilon_H$ ) associated  
392 with  $\text{SO}_4$ -AOM at the SMTZ using the Rayleigh distillation function (Crowe et al., 2011; Egger et al., 2015b;  
393 Rayleigh, 1896; Whiticar, 1999). Corresponding estimates for  $\epsilon_C$  of  $\sim 8 \text{ ‰}$  ( $R^2 = 0.972$ ) and  $\epsilon_H$  of  $\sim 58 \text{ ‰}$  ( $R^2 =$   
394  $0.982$ ) are at the lower end of previously documented values in marine and brackish-marine environments ( $8\text{-}38 \text{ ‰}$   
395 for  $\epsilon_C$  and  $100\text{-}324 \text{ ‰}$  for  $\epsilon_H$ ) (Alperin et al., 1988; Egger et al., 2015b; Holler et al., 2009; Martens et al., 1999;  
396 Reeburgh, 2007). At the base of the SMTZ, however, upward diffusing  $\text{CH}_4$  reveals an initial depletion in  $\delta^{13}\text{C-CH}_4$   
397 (Fig. 4). Such a shift to  $^{13}\text{C}$ -depleted  $\text{CH}_4$  together with a decrease in its concentration could indicate an enzyme-  
398 mediated equilibrium C isotope exchange during  $\text{SO}_4$ -AOM at low  $\text{SO}_4^{2-}$  concentrations ( $< 0.5 \text{ mM}$ ) (Holler et al.,  
399 2012; Yoshinaga et al., 2014). The effect of such mechanisms on deuterated  $\text{CH}_4$  is likely limited.

#### 400 4.1.3 Cryptic S cycling

401 Earlier studies postulated ongoing  $\text{SO}_4^{2-}$  reduction ( $< 1 \text{ nmol cm}^{-3} \text{ d}^{-1}$ ) within the  $\text{SO}_4^{2-}$ -depleted ( $< 0.5 \text{ mM}$ ) limnic  
402 deposits below the SMTZ in sediments of the Black Sea (Holmkvist et al., 2011b; Knab et al., 2009; Leloup et al.,  
403 2007), Baltic Sea (Holmkvist et al., 2011a, 2014; Leloup et al., 2009) and Alaskan Beaufort Sea (Treude et al., 2014)  
404 likely driven by  $\text{SO}_4^{2-}$  production from re-oxidation of dissolved sulfide with oxidized Fe minerals. In this  
405 mechanism, Fe oxides enhance the recycling of sulfide to  $\text{SO}_4^{2-}$  in a cryptic S cycle (Holmkvist et al., 2011a; Treude  
406 et al., 2014) thereby fueling  $\text{SO}_4^{2-}$ -driven AOM in Fe oxide-rich sediments. In this cryptic S cycle, dissolved sulfide  
407 is oxidized to zero-valent sulfur ( $\text{S}_0$ ), a key intermediate in AOM, which is subsequently disproportionated to  $\text{SO}_4^{2-}$   
408 and sulfide by associated Deltaproteobacteria (Holmkvist et al., 2011a; Milucka et al., 2012; Sivan et al., 2014;  
409 Treude et al., 2014). The additional  $\text{SO}_4^{2-}$ , produced during  $\text{S}_0$  disproportionation, may then be re-used by the  
410 methanotrophic archaea as an electron acceptor for  $\text{SO}_4$ -AOM (Milucka et al., 2012).

411 Our model results suggest slow rates of ongoing  $\text{SO}_4^{2-}$  reduction of  $< 0.2 \text{ nmol cm}^{-3} \text{ d}^{-1}$  (Fig. 6) within the limnic  
412 deposits exposed to dissolved sulfide (Table 6), in line with estimated SRR based on  $^{35}\text{SO}_4^{2-}$  incubation experiments  
413 with Black Sea sediments from below the SMTZ of  $\sim 0.1\text{-}0.5 \text{ nmol cm}^{-3} \text{ d}^{-1}$  (Knab et al., 2009; Leloup et al., 2007).  
414 Below the sulfidization front, SRR drop to  $\sim 2 \text{ pmol cm}^{-3} \text{ d}^{-1}$ , but remain above zero. Active  $\text{SO}_4^{2-}$  reduction in these  
415  $\text{SO}_4^{2-}$ -depleted sediments requires deep  $\text{SO}_4^{2-}$  formation to maintain low net rates of  $\text{SO}_4^{2-}$  reduction. In the model,  $\text{S}_0$   
416 disproportionation is the only potential source of pore water  $\text{SO}_4^{2-}$  at depth (Table 3). Formation of  $\text{S}_0$ , in turn, occurs  
417 exclusively by oxidation of dissolved sulfide during the reductive dissolution of Fe oxides, explaining the distinct  $\text{S}_0$   
418 disproportionation peak of  $\sim 60 \text{ pmol cm}^{-3} \text{ d}^{-1}$  around the sulfidization front (Fig. 6). Thus, based on the model  
419 assumptions, we conclude that Fe oxides increase the transformation of sulfide to  $\text{SO}_4^{2-}$  via formation and subsequent  
420 disproportionation of  $\text{S}_0$  in these sediments, as suggested previously (Holmkvist et al., 2011b; Knab et al., 2009;  
421 Leloup et al., 2007). Such recycling of  $\text{SO}_4^{2-}$  stimulates slow rates of  $\text{SO}_4$ -AOM in the sediments below the SMTZ,  
422 explaining the low background rates of  $\text{SO}_4^{2-}$  reduction throughout the limnic deposits at depth ( $\sim 2 \text{ pmol cm}^{-3} \text{ d}^{-1}$ ).  
423 These results support recent findings of indirect Fe stimulated  $\text{SO}_4^{2-}$  driven AOM in laboratory experiments (Sivan et  
424 al., 2014), and highlight that Fe oxides could play a significant role as stimulators of AOM and S recycling in natural  
425 environments.



#### 426 **4.2 Fe reduction below the sulfidization front**

427 Below the sulfidization front,  $\text{Fe}^{2+}$  starts to accumulate in the pore water (Fig. 3). Although previous studies have  
428 also reported an increase of dissolved  $\text{Fe}^{2+}$  around the depth where sulfide levels drop below the detection limit  
429 (Holmkvist et al., 2011b; Jørgensen et al., 2004; Knab et al., 2009), the source of this pore water  $\text{Fe}^{2+}$  has remained  
430 unknown. One possible explanation could be that the elevated  $\text{Fe}^{2+}$  concentrations at depth represent remnant  $\text{Fe}^{2+}$   
431 accumulated during the Black Sea “Lake” phase (Knab et al., 2009). In our model,  $\text{Fe}^{2+}$  shows a broad peak of  $\sim 300$   
432  $\mu\text{M}$  until  $\sim 300$  cm depth in the sediment during the initial Lake phase, assuming organoclastic Fe reduction as the  
433 only Fe reduction pathway (data not shown). The removal of  $\text{Fe}^{2+}$  through authigenic formation of reduced Fe(II)  
434 minerals, however, prevents the accumulation of substantial amounts of  $\text{Fe}^{2+}$  in the pore water below  $\sim 300$  cm  
435 sediment depth during the Lake phase (Fig. 8). We therefore conclude that the high concentrations of dissolved  $\text{Fe}^{2+}$   
436 below the sulfidization front are most likely indicative of active Fe reduction in these sediments.

#### 437 **4.2.1 Fe reduction through cryptic S cycling**

438 In theory, a cryptic S cycle, as described in section 4.1.3, could result in net accumulation of dissolved  $\text{Fe}^{2+}$  if the  
439 sulfide consumption from reaction with ferric Fe outweighs the production of sulfide from  $\text{SO}_4^{2-}$  reduction. Modeled  
440  $\text{Fe}^{2+}$  indeed shows a peak of  $< 100 \mu\text{M}$  directly below the sulfidization front, assuming no active Fe reduction in the  
441 limnic deposits (Fig. 8). However, concentrations of dissolved  $\text{Fe}^{2+}$  are too low compared to the measurements and  
442 confined to sediments between 300 – 400 cm depths only. The diagenetic model developed in this study therefore  
443 suggests that cryptic S cycling cannot explain the high concentrations of dissolved  $\text{Fe}^{2+}$  in the deep limnic deposits.

#### 444 **4.2.2 Organoclastic Fe reduction**

445 In the model, the reduction of Fe oxides coupled to organic matter degradation only occurs with the easily reducible  
446  $\alpha$  phase in order to allow for the burial of the more crystalline  $\beta$  phase at depth (Table 3) (Rooze et al., 2016). Since  
447 the  $\alpha$  phase is efficiently reduced in the upper few centimeters during organoclastic Fe reduction, no easily reducible  
448 Fe oxides are being buried into the deep sediments in the diagenetic model. Organoclastic Fe reduction therefore  
449 does not occur within the modeled deep limnic deposits that exclusively contain more crystalline ( $\beta$ ) and refractory  
450 ( $\gamma$ ) Fe oxides (Fig. 5). Instead, we assume that  $\text{CH}_4$  represents a plausible electron donor for the reduction of more  
451 crystalline Fe oxides in the organic-poor deep sediments with relatively refractory old organic matter ( $< 0.8$  wt %).  
452 This assumption is supported by an increasing body of geochemical evidence and laboratory incubation experiments  
453 showing that Fe-AOM might be occurring in a variety of different aquatic environments (Amos et al., 2012; Beal et  
454 al., 2009; Crowe et al., 2011; Egger et al., 2015b; Riedinger et al., 2014; Scheller et al., 2016; Segarra et al., 2013;  
455 Sivan et al., 2011; Wankel et al., 2012).

456 In addition, several studies have shown that Fe-reducing microorganisms are able to outcompete methanogens for  
457 common substrates (e.g. acetate and  $\text{H}_2$ ), thus reducing the concentrations of these common primary electron donors  
458 to levels that are too low for methanogens to grow (Acht nich et al., 1995; Lovley and Phillips, 1987; Lovley et al.,  
459 1989). These results, together with the observed capability of methanogens to switch from  $\text{CH}_4$  production to Fe  
460 reduction (Bodegom et al., 2004; Bond and Lovley, 2002; Liu et al., 2011; Reiche et al., 2008; Sivan et al., 2016;



461 Vargas et al., 1998) led to the common conclusion that Fe oxides exert a suppressive effect on methanogenesis.  
462 Ongoing CH<sub>4</sub> production in the Fe oxide-rich limnic deposits, as deduced from the isotopic composition of pore  
463 water CH<sub>4</sub> (Fig. 4) could then indicate limited organoclastic Fe reduction in these sediments.

464 However, there is increasing evidence that (semi)conductive crystalline Fe oxides (e.g. hematite and magnetite) can,  
465 in fact, stimulate concurrent methanogenesis and organoclastic Fe reduction through direct interspecies electron  
466 transfer (DIET), by serving as electron conduits among syntrophic CH<sub>4</sub>-producing organisms at rates that are  
467 substantially higher than those for interspecies electron transfer by H<sub>2</sub> (Cruz Viggi et al., 2014; Kato et al., 2012; Li  
468 et al., 2014; Zhou et al., 2014; Zhuang et al., 2015). The inhibitory effect of Fe reduction on methanogenesis thus  
469 appears to be lower for crystalline Fe oxides such as hematite and magnetite, which are less bioavailable to Fe-  
470 reducing organisms than poorly crystalline (amorphous) Fe oxides (e.g. ferrihydrite and lepidocrocite) (Lovley,  
471 1991; Qu et al., 2004; Zhuang et al., 2015). These findings indicate that the crystallinity and conductivity of Fe  
472 oxides may play a key role in determining whether methanogenesis is stimulated or suppressed in Fe oxide-rich  
473 environments.

474 The presence of methanogens that are able to rapidly switch between methanogenesis and reduction of Fe oxides  
475 could also result in a reactivation of less reactive Fe oxides that were not reduced during initial organoclastic Fe  
476 reduction in the deep methanogenic zone as suggested by Sivan et al. (2016). Thus, the deep limnic sediments may  
477 be characterized by a complex interplay of concurrent methanogenesis, Fe oxide reduction and methanotrophy, i.e.  
478 AOM.

#### 479 4.2.3 Fe-AOM

480 Our model results indicate that Fe-AOM could also be a possible mechanism explaining the buildup of pore water  
481 Fe<sup>2+</sup> below the sulfidization front. Previous studies have shown that in systems where production and oxidation of  
482 CH<sub>4</sub> take place concurrently, methanogenesis might conceal the isotopic signature of AOM (Egger et al., 2015b;  
483 Seifert et al., 2006; Whiticar, 1999). Thus, unlike SO<sub>4</sub>-AOM, Fe-dependent AOM likely only has little effect on the  
484 isotopic composition of pore water CH<sub>4</sub> due to the removal of small amounts of CH<sub>4</sub> in sediments with ongoing  
485 methanogenesis. This might explain why pore water CH<sub>4</sub> does not show enrichment in both heavy isotopes below the  
486 sulfidization front as would be expected if Fe-AOM would occur, but rather indicates antipathetic changes, i.e.  
487 depletion in <sup>13</sup>C-CH<sub>4</sub> and enrichment in D-CH<sub>4</sub>, usually attributed to CH<sub>4</sub> production from carbonate reduction  
488 (Chanton et al., 2005; Whiticar, 1999).

489 Model derived rates for Fe-AOM of ~ 0.1 pmol cm<sup>-3</sup> d<sup>-1</sup> (Fig. 6) are significantly lower than potential Fe-AOM rates  
490 of ~ 4 nmol cm<sup>-3</sup> d<sup>-1</sup> estimated from laboratory incubation studies (Egger et al., 2015b; Segarra et al., 2013; Sivan et  
491 al., 2011) with brackish and limnic sediment samples. This large deviation is likely due to an overestimation of Fe-  
492 AOM rates derived from stimulated microbial communities under laboratory conditions using freshly synthesized  
493 and thus easily bioavailable Fe oxides when compared to in-situ conditions.

494 In the upper 800 cm of sediment, Fe-AOM accounts for < 0.1 % of total CH<sub>4</sub> oxidation, with the remaining > 99.9 %  
495 attributed to SO<sub>4</sub>-AOM (Table 6). Below the sulfidization front, Fe-AOM contributes to ~ 10 % of total CH<sub>4</sub>  
496 removal. However, while high rates of SO<sub>4</sub>-AOM are mainly restricted to the SMTZ, Fe-AOM might occur over a



497 deep methanogenic zone, reaching far down into the sediment. To accurately assess the contribution of Fe-AOM to  
498 the total CH<sub>4</sub> consumption in Black Sea sediments, additional knowledge about the vertical expansion of the Fe  
499 oxide-rich limnic sediments deposited during the Black Sea “Lake” phase would be required.

#### 500 **4.3 Impact of S-Fe-CH<sub>4</sub> dynamics on sedimentary P diagenesis**

501 Degradation of organic matter and the subsequent release of HPO<sub>4</sub><sup>2-</sup> to the pore water during early diagenesis  
502 typically results in a sink-switching from organic P to authigenic P-bearing phases such as Ca phosphates (Filippelli,  
503 1997; Ruttenger and Berner, 1993; Slomp et al., 1996a), Mn-Ca carbonates (Jilbert and Slomp, 2013; Mort et al.,  
504 2010; Suess, 1979) or reduced Fe phosphates (Burns, 1997; Jilbert and Slomp, 2013; Martens et al., 1978; März et  
505 al., 2008). Reductive dissolution of Fe oxides by dissolved sulfide and the following liberation of HPO<sub>4</sub><sup>2-</sup> may also  
506 contribute to the buildup of pore water HPO<sub>4</sub><sup>2-</sup> (Burns, 1997; Egger et al., 2015a; März et al., 2008; Schulz et al.,  
507 1994). Thus, the downward sulfidization ultimately results in the accumulation of dissolved HPO<sub>4</sub><sup>2-</sup> in the pore water  
508 as the sulfidization front moves downward into the limnic deposits (Fig. 7).

509 The pore water profile of HPO<sub>4</sub><sup>2-</sup> (Fig. 3) indicates the presence of a sink for HPO<sub>4</sub><sup>2-</sup> below the sulfidization front  
510 and, to a lesser extent, in the sulfidic sediments around the SMTZ, likely unrelated to Ca-P authigenesis (Fig. 5).  
511 Such a sink for HPO<sub>4</sub><sup>2-</sup> below sulfidic sediments has been observed previously (Burns, 1997; Egger et al., 2015a;  
512 März et al., 2008; Schulz et al., 1994; Slomp et al., 2013) and shown to be most likely the result of vivianite  
513 formation (Egger et al., 2015a; Hsu et al., 2014; März et al., 2008). Abundant dissolved Fe<sup>2+</sup> and a peak in Fe-  
514 associated P below the sulfidization front observed in this study (Fig. 3 and Fig. 5) suggest that vivianite authigenesis  
515 might also be occurring in the limnic deposits below the sulfidization front in Black Sea sediments.

516 Assuming that vivianite formation represents the only sink for pore water HPO<sub>4</sub><sup>2-</sup> results in a good fit between the  
517 modeled and measured pore water profile of HPO<sub>4</sub><sup>2-</sup> below the sulfidization front (Fig. 3). Modeled vivianite  
518 formation accounts for up to 70 % of total Fe-associated P directly below the sulfidization front. However, the model  
519 underestimates the sharp peak in Fe-associated P directly below the sulfidization front, suggesting that modeled  
520 vivianite formation likely underestimates the actual contribution of vivianite in these sediments. In the limnic  
521 deposits not yet impacted by the downward sulfidization, modeled vivianite accounts for ~ 20 – 30 % of total Fe-  
522 associated P. From this, we estimate that vivianite may be responsible for > 20 % of total P burial directly below the  
523 sulfidization front and for ~ 10 % of total P burial in the deep limnic deposits at depth.

524 Running the model without Fe-AOM and thus without a source of dissolved Fe<sup>2+</sup> at depth results in a modeled  
525 vertical HPO<sub>4</sub><sup>2-</sup> pore water profile of ~ 300 μM at depth in the sediment (Fig. 8). This suggests that Fe-AOM can  
526 promote conditions that allow sequestration of a significant proportion of P as vivianite in the limnic deposits below  
527 the sulfidization front. Consistent with earlier findings, Fe-AOM likely only accounts for a small fraction of total  
528 CH<sub>4</sub> oxidation, but may substantially impact the biogeochemical cycling of sedimentary P (Egger et al., 2015a,  
529 2015b; Rooze et al., 2016).

530 The deviation between the modeled and measured profiles of HPO<sub>4</sub><sup>2-</sup> and Fe-associated P around the SMTZ (Fig. 3  
531 and Fig. 5) could indicate the formation of vivianite in microenvironments as previously suggested for sulfidic  
532 sediments (Dijkstra et al., 2014; Jilbert and Slomp, 2013). For example, *Deltaproteobacteria*, known to be involved



533 in  $\text{SO}_4$ -AOM, have been shown to accumulate Fe- and P-rich inclusions in their cells (Milucka et al., 2012). They  
534 may therefore provide a potential explanation for the occurrence of Fe-associated P in sulfidic sediments (Dijkstra et  
535 al., 2014; Jilbert and Slomp, 2013). However, such microenvironments are not captured in our model.

536 In the diagenetic model, vivianite undergoes dissolution if sulfide is present in the pore waters (Table 3). Sulfide-  
537 induced vivianite dissolution significantly improved the model fit to the measured  $\text{HPO}_4^{2-}$  and sulfide data. With the  
538 downward migration of dissolved sulfide, modeled vivianite becomes increasingly enriched below the sulfidization  
539 front (Fig. 7). Thus, similar to the sulfidization front, a downward diffusive vivianite front may exist in sedimentary  
540 systems experiencing downward sulfidization.

541 In summary, the enhanced downward sulfidization driven by  $\text{SO}_4$ -AOM leads to dissolution of Fe oxide-bound P in  
542 the lake deposits. Below the sulfidization front, downward diffusing  $\text{HPO}_4^{2-}$  is bound again in authigenic vivianite  
543 due to high concentrations of dissolved  $\text{Fe}^{2+}$  at depth in the sediment generated by ongoing Fe oxide reduction. As a  
544 result, trends in total P with depth are significantly altered, showing an accumulation in total P below the  
545 sulfidization front unrelated to changes in organic matter deposition and enhanced sedimentary P burial during  
546 deposition.

## 547 5. Conclusions

548 In the Black Sea, the shift from a freshwater lake to a marine system and subsequent downward diffusion of marine  
549  $\text{SO}_4^{2-}$  into the  $\text{CH}_4$ -bearing lake sediments results in a multitude of diagenetic reactions around the SMTZ (Fig. 9).  
550 The diagenetic model developed in this study shows that  $\text{SO}_4$ -AOM within the SMTZ significantly enhances the  
551 downward diffusive flux of sulfide into the deep limnic deposits, forming a distinct diagenetic sulfidization front  
552 around 300 cm depth in the sediment. Our results indicate that without this additional source of dissolved sulfide in  
553 the SMTZ, the current sulfidization front would be located around a depth of 150 cm. During the downward  
554 sulfidization, Fe oxides, Fe carbonates and vivianite are converted to Fe sulfide phases, leading to an enrichment in  
555 solid phase S contents and the release of  $\text{HPO}_4^{2-}$  to the pore water. Our results further support the hypothesis that part  
556 of the downward migrating sulfide is re-oxidized to  $\text{SO}_4^{2-}$  upon reaction with ferric Fe minerals, fueling a cryptic S  
557 cycle and thus stimulating slow rates ( $\sim 2 \text{ pmol cm}^{-3} \text{ d}^{-1}$ ) of  $\text{SO}_4$ -AOM in the  $\text{SO}_4^{2-}$ -depleted limnic deposits below  
558 the SMTZ (Holmkvist et al., 2011a, 2011b; Knab et al., 2009; Leloup et al., 2007).

559 We propose that besides organoclastic Fe oxide reduction, AOM coupled to the reduction of Fe oxides may also be a  
560 possible mechanism explaining the high concentrations of  $\text{Fe}^{2+}$  in the pore water below the sulfidization front. The  
561 buildup of dissolved  $\text{Fe}^{2+}$  at depth creates conditions that allow sequestration of the downward diffusing  $\text{HPO}_4^{2-}$  as  
562 authigenic vivianite, resulting in an accumulation of total P in these sediments.

563 The diagenetic processes described here reveal that AOM may strongly overprint burial records of Fe, S and P in  
564 depositional marine systems subject to changes in organic matter loading or water column salinity such as coastal  
565 environments (Egger et al., 2015a; Rooze et al., 2016), deep-sea fan sediments (März et al., 2008; Schulz et al.,  
566 1994) and many high-latitude seas (Holmkvist et al., 2014; Treude et al., 2014). Interpreting these diagenetic patterns  
567 as primary sedimentary signals may lead to incorrect reconstructions of environmental conditions during sediment  
568 deposition.



569 **Acknowledgments**

570 We thank the captain, crew and shipboard party of the PHOXY cruise aboard R/V Pelagia to the Black Sea in June  
571 2013. We also thank NIOZ Marine Research Facilities for their support and K. Bakker and S. Ossebaar for their  
572 contribution to the pore water analysis. D. van de Meent, T. Claessen, T. Zalm, A. van Dijk, E. Dekker and G.  
573 Megens are acknowledged for technical and analytical assistance in Utrecht. We further thank C. van der Veen for  
574 the methane isotope analysis. This research was funded by ERC Starting Grant 278364, NWO Open Competition  
575 Grant 822.01013 and NWO-Vici Grant 865.13.005 (to C. P. Slomp). This work was carried out under the program of  
576 the Netherlands Earth System Science Centre (NESSC), financially supported by the Ministry of Education, Culture  
577 and Science (OCW).  
578

579 **References**

- 580 Achtnich, C., Bak, F. and Conrad, R.: Competition for electron donors among nitrate reducers, ferric iron reducers,  
581 sulfate reducers, and methanogens in anoxic paddy soil, *Biol. Fertil. Soils*, 19, 65–72, 1995.
- 582 Alperin, M. J., Reeburgh, W. S. and Whiticar, M. J.: Carbon and hydrogen isotope fractionation resulting from  
583 anaerobic methane oxidation, *Glob. Biogeochem. Cycl.*, 2(3), 279–288, 1988.
- 584 Amos, R. T., Bekins, B. A., Cozzarelli, I. M., Voytek, M. A., Kirshtein, J. D., Jones, E. J. P. and Blowes, D. W.:  
585 Evidence for iron-mediated anaerobic methane oxidation in a crude oil-contaminated aquifer, *Geobiology*, 10(6),  
586 506–17, 2012.
- 587 Arthur, M. A. and Dean, W. E.: Organic-matter production and evolution of anoxia in the Holocene Black Sea,  
588 *Paleoceanography*, 13(4), 395–411, 1998.
- 589 Beal, E. J., House, C. H. and Orphan, V. J.: Manganese- and iron-dependent marine methane oxidation, *Science*,  
590 325(5937), 184–187, 2009.
- 591 Berg, P., Rysgaard, S. and Thamdrup, B.: Dynamic modeling of early diagenesis and nutrient cycling. A case study  
592 in an Arctic marine sediment, *Am. J. Sci.*, 303(10), 905–955, 2003.
- 593 Berner, R. A.: *Early Diagenesis: A Theoretical Approach*, Princeton University Press., 1980.
- 594 Bodegom, P. M., Scholten, J. C. M. and Stams, A. J. M.: Direct inhibition of methanogenesis by ferric iron, *FEMS*  
595 *Microbiol. Ecol.*, 49(2), 261–268, 2004.
- 596 Bond, D. R. and Lovley, D. R.: Reduction of Fe(III) oxide by methanogens in the presence and absence of  
597 extracellular quinones, *Environ. Microbiol.*, 4(2), 115–24, 2002.
- 598 Boudreau, B. P.: The diffusive tortuosity of fine-grained unlithified sediments, *Geochim. Cosmochim. Acta*, 60(16),  
599 3139–3142, 1996.
- 600 Boudreau, B. P.: Diagenetic models and their implementation. Modelling transport and reactions in aquatic  
601 sediments., 1997.



- 602 Brass, M. and Röckmann, T.: Continuous-flow isotope ratio mass spectrometry method for carbon and hydrogen  
603 isotope measurements on atmospheric methane, *Atmos. Meas. Tech.*, 3(6), 1707–1721, 2010.
- 604 Burns, S. J.: Early diagenesis in Amazon fan sediments, in *Proceeding of the Ocean Drilling Program, Scientific*  
605 *Results*, vol. 155, edited by R. D. Flood, D. J. W. Piper, A. Klaus, and L. C. Peterson, pp. 497–504., 1997.
- 606 Burton, E. D., Sullivan, L. A., Bush, R. T., Johnston, S. G. and Keene, A. F.: A simple and inexpensive chromium-  
607 reducible sulfur method for acid-sulfate soils, *Appl. Geochemistry*, 23(9), 2759–2766, 2008.
- 608 Capet, A., Beckers, J.-M. and Grégoire, M.: Drivers , mechanisms and long-term variability of seasonal hypoxia on  
609 the Black Sea northwestern shelf – is there any recovery after eutrophication?, *Biogeosciences*, 10, 3943–3962,  
610 2013.
- 611 Chanton, J., Chaser, L., Glasser, P. and Siegel, D.: Carbon and hydrogen isotopic effects in microbial methane from  
612 terrestrial environments, in *Stable isotopes and biosphere-atmosphere interactions*, edited by L. Flanagan, pp. 85–  
613 105, Elsevier-Academic Press., Amsterdam., 2005.
- 614 Claff, S. R., Sullivan, L. A., Burton, E. D. and Bush, R. T.: A sequential extraction procedure for acid sulfate soils:  
615 Partitioning of iron, *Geoderma*, 155, 224–230, 2010.
- 616 Crowe, S. A., Katsev, S., Leslie, K., Sturm, A., Magen, C., Nomosatryo, S., Pack, M. A., Kessler, J. D., Reeburgh,  
617 W. S., Roberts, J. A., González, L., Douglas Haffner, G., Mucci, A., Sundby, B. and Fowle, D. A.: The methane  
618 cycle in ferruginous Lake Matano, *Geobiology*, 9(1), 61–78, 2011.
- 619 Cruz Viggì, C., Rossetti, S., Fazi, S., Paiano, P., Majone, M. and Aulenta, F.: Magnetite particles triggering a faster  
620 and more robust syntrophic pathway of methanogenic propionate degradation, *Environ. Sci. Technol.*, 48(13), 7536–  
621 7543, 2014.
- 622 Degens, E. T. and Ross, D. A.: *The Black Sea - Geology, Chemistry, and Biology: American Association of*  
623 *Petroleum Geologists Memoir 20*, 1974.
- 624 Dijkstra, N., Kraal, P., Kuypers, M. M. M., Schnetger, B. and Slomp, C. P.: Are iron-phosphate minerals a sink for  
625 phosphorus in anoxic Black Sea sediments?, *PLoS One*, 9(7), 2014.
- 626 Eckert, S., Brumsack, H.-J., Severmann, S., Schnetger, B., März, C. and Frollje, H.: Establishment of euxinic  
627 conditions in the Holocene Black Sea, *Geology*, 41(4), 431–434, 2013.
- 628 Egger, M., Jilbert, T., Behrends, T., Rivard, C. and Slomp, C. P.: Vivianite is a major sink for phosphorus in  
629 methanogenic coastal surface sediments, *Geochim. Cosmochim. Acta*, 169, 217–235, 2015a.
- 630 Egger, M., Rasigraf, O., Sapart, C. J., Jilbert, T., Jetten, M. S. M., Röckmann, T., van der Veen, C., Bändä, N.,  
631 Kartal, B., Ettwig, K. F. and Slomp, C. P.: Iron-Mediated Anaerobic Oxidation of Methane in Brackish Coastal  
632 Sediments, *Environ. Sci. Technol.*, 49(1), 277–283, 2015b.
- 633 Ettwig, K. F., Butler, M. K., Le Paslier, D., Pelletier, E., Mangenot, S., Kuypers, M. M. M., Schreiber, F., Dutilh, B.  
634 E., Zedelius, J., de Beer, D., Gloerich, J., Wessels, H. J. C. T., van Alen, T., Luesken, F., Wu, M. L., van de Pas-  
635 Schoonen, K. T., Op den Camp, H. J. M., Janssen-Megens, E. M., Francoijs, K.-J., Stunnenberg, H., Weissenbach, J.,



- 636 Jetten, M. S. M. and Strous, M.: Nitrite-driven anaerobic methane oxidation by oxygenic bacteria, *Nature*,  
637 464(7288), 543–8, 2010.
- 638 Filippelli, G. M.: Controls on phosphorus concentration and accumulation in oceanic sediments, *Mar. Geol.*, 139(1–  
639 4), 231–240, 1997.
- 640 Froelich, P. N., Klinkhammer, G. P., Bender, M. L., Luedtke, N. A., Heath, G. R., Cullen, D., Dauphin, P.,  
641 Hammond, D., Hartman, B. and Maynard, V.: Early oxidation of organic matter in pelagic sediments of the eastern  
642 equatorial Atlantic : suboxic diagenesis, *Geochim. Cosmochim. Acta*, 43, 1075–1090, 1979.
- 643 Hindmarsh, A. C.: ODEPACK, A Systematized Collection of ODE Solvers, in *IMACS Transactions on Scientific  
644 Computation*, Vol. 1, edited by R. S. Stepleman and Others, pp. 55–64, North-Holland, Amsterdam., 1983.
- 645 Holler, T., Wegener, G., Knittel, K., Boetius, A., Brunner, B., Kuypers, M. M. M. and Widdel, F.: Substantial (13)  
646 C/(12) C and D/H fractionation during anaerobic oxidation of methane by marine consortia enriched in vitro,  
647 *Environ. Microbiol. Rep.*, 1(5), 370–6, 2009.
- 648 Holler, T., Wegener, G., Niemann, H., Ferdelman, T. G., Boetius, A., Kristiansen, T. Z., Molina, H., Pandey, A.,  
649 Werner, J. K., Juluri, K. R., Xu, Y., Glenn, D., Parang, K. and Snyder, S. H.: Carbon and sulfur back flux during  
650 anaerobic microbial oxidation of methane and coupled sulfate reduction, *Proc. Natl. Acad. Sci.*, 109(51), 21170–  
651 21170, doi:10.1073/pnas.1218683109, 2012.
- 652 Holmkvist, L., Ferdelman, T. G. and Jørgensen, B. B.: A cryptic sulfur cycle driven by iron in the methane zone of  
653 marine sediment (Aarhus Bay, Denmark), *Geochim. Cosmochim. Acta*, 75(12), 3581–3599, 2011a.
- 654 Holmkvist, L., Kamysny, A., Brüchert, V., Ferdelman, T. G. and Jørgensen, B. B.: Sulfidization of lacustrine  
655 glacial clay upon Holocene marine transgression (Arkona Basin, Baltic Sea), *Geochim. Cosmochim. Acta*, 142, 75–  
656 94, 2014.
- 657 Holmkvist, L., Kamysny, A., Vogt, C., Vamvakopoulos, K., Ferdelman, T. G. and Jørgensen, B. B.: Sulfate  
658 reduction below the sulfate–methane transition in Black Sea sediments, *Deep Sea Res. Part I Oceanogr. Res. Pap.*,  
659 58(5), 493–504, 2011b.
- 660 Hsu, T.-W., Jiang, W.-T. and Wang, Y.: Authigenesis of vivianite as influenced by methane-induced sulfidization in  
661 cold-seep sediments off southwestern Taiwan, *J. Asian Earth Sci.*, 89, 88–97, 2014.
- 662 Jilbert, T. and Slomp, C. P.: Iron and manganese shuttles control the formation of authigenic phosphorus minerals in  
663 the euxinic basins of the Baltic Sea, *Geochim. Cosmochim. Acta*, 107, 155–169, 2013.
- 664 Jørgensen, B. B., Böttcher, M. E., Lüschen, H., Neretin, L. N. and Volkov, I. I.: Anaerobic methane oxidation and a  
665 deep H<sub>2</sub>S sink generate isotopically heavy sulfides in Black Sea sediments, *Geochim. Cosmochim. Acta*, 68(9),  
666 2095–2118, 2004.
- 667 Jørgensen, B. B., Weber, A. and Zopfi, J.: Sulfate reduction and anaerobic methane oxidation in Black Sea  
668 sediments, *Deep Sea Res. Part I Oceanogr. Res. Pap.*, 48, 2097–2120, 2001.
- 669 Kato, S., Hashimoto, K. and Watanabe, K.: Methanogenesis facilitated by electric syntrophy via (semi)conductive  
670 iron-oxide minerals, *Environ. Microbiol.*, 14(7), 1646–1654, 2012.



- 671 Kemp, W. M., Testa, J. M., Conley, D. J., Gilbert, D. and Hagy, J. D.: Temporal responses of coastal hypoxia to  
672 nutrient loading and physical controls, *Biogeosciences*, 6, 2985–3008, 2009.
- 673 Knab, N. J., Cragg, B. A., Hornibrook, E. R. C., Holmkvist, L., Pancost, R. D., Borowski, C., Parkes, R. J. and  
674 Jørgensen, B. B.: Regulation of anaerobic methane oxidation in sediments of the Black Sea, *Biogeosciences*, (6),  
675 1505–1518, 2009.
- 676 Knittel, K. and Boetius, A.: Anaerobic oxidation of methane: progress with an unknown process, *Annu. Rev.*  
677 *Microbiol.*, 63, 311–334, 2009.
- 678 Kraal, P. and Slomp, C. P.: Rapid and extensive alteration of phosphorus speciation during oxic storage of wet  
679 sediment samples, *PLoS One*, 9(5), e96859, 2014.
- 680 Kraal, P., Slomp, C. P., Forster, A. and Kuypers, M. M. M.: Pyrite oxidation during sample storage determines  
681 phosphorus fractionation in carbonate-poor anoxic sediments, *Geochim. Cosmochim. Acta*, 73(11), 3277–3290,  
682 2009.
- 683 Leloup, J., Fossing, H., Kohls, K., Holmkvist, L., Borowski, C. and Jørgensen, B. B.: Sulfate-reducing bacteria in  
684 marine sediment (Aarhus Bay, Denmark): abundance and diversity related to geochemical zonation, *Environ.*  
685 *Microbiol.*, 11(5), 1278–1291, 2009.
- 686 Leloup, J., Loy, A., Knab, N. J., Borowski, C., Wagner, M. and Jørgensen, B. B.: Diversity and abundance of sulfate-  
687 reducing microorganisms in the sulfate and methane zones of a marine sediment, Black Sea, *Environ. Microbiol.*,  
688 9(1), 131–142, 2007.
- 689 Li, H., Chang, J., Liu, P., Fu, L., Ding, D. and Lu, Y.: Direct interspecies electron transfer accelerates syntrophic  
690 oxidation of butyrate in paddy soil enrichments, *Environ. Microbiol.*, 17, 1–45, 2014.
- 691 Liu, D., Wang, H., Dong, H., Qiu, X., Dong, X. and Cravotta, C. A.: Mineral transformations associated with  
692 goethite reduction by *Methanosarcina barkeri*, *Chem. Geol.*, 288(1-2), 53–60, 2011.
- 693 Lovley, D. R.: Dissimilatory Fe(III) and Mn(IV) reduction., *Microbiol. Rev.*, 55(2), 259–287, 1991.
- 694 Lovley, D. R. and Phillips, E. J. P.: Competitive mechanisms for inhibition of sulfate reduction and methane  
695 production in the zone of ferric iron reduction in sediments, *Appl. Environ. Microbiol.*, 53(11), 1987.
- 696 Lovley, D. R., Phillips, E. J. P. and Lonergan, D. J.: Hydrogen and formate oxidation coupled to dissimilatory  
697 reduction of iron or manganese by *Alteromonas putrefaciens*, *Appl. Environ. Microbiol.*, 55(3), 700–706, 1989.
- 698 Martens, C. S., Albert, D. B. and Alperin, M. J.: Stable isotope tracing of anaerobic methane oxidation in the gassy  
699 sediments of Eckernforde Bay, German Baltic Sea, *Am. J. Sci.*, 299, 589–610, 1999.
- 700 Martens, C. S., Berner, R. A. and Rosenfeld, J. K.: Interstitial water chemistry of anoxic Long Island Sound  
701 sediments. 2. Nutrient regeneration and phosphate removal, *Limnol. Oceanogr.*, 23(4), 605–617, 1978.
- 702 März, C., Hoffmann, J., Bleil, U., de Lange, G. J. and Kasten, S.: Diagenetic changes of magnetic and geochemical  
703 signals by anaerobic methane oxidation in sediments of the Zambezi deep-sea fan (SW Indian Ocean), *Mar. Geol.*,  
704 255(3-4), 118–130, 2008.



- 705 Meysman, F. J. R., Boudreau, B. P. and Middelburg, J. J.: Modeling reactive transport in sediments subject to  
706 bioturbation and compaction, *Geochim. Cosmochim. Acta*, 69(14), 3601–3617, 2005.
- 707 Milucka, J., Ferdelman, T. G., Polerecky, L., Franzke, D., Wegener, G., Schmid, M., Lieberwirth, I., Wagner, M.,  
708 Widdel, F. and Kuypers, M. M. M.: Zero-valent sulphur is a key intermediate in marine methane oxidation, *Nature*,  
709 491(7425), 541–6, 2012.
- 710 Moodley, L., Middelburg, J. J., Herman, P. M. J., Soetaert, K. and de Lange, G. J.: Oxygenation and organic-matter  
711 preservation in marine sediments: Direct experimental evidence from ancient organic carbon-rich deposits, *Geology*,  
712 33(11), 889, 2005.
- 713 Mort, H. P., Slomp, C. P., Gustafsson, B. G. and Andersen, T. J.: Phosphorus recycling and burial in Baltic Sea  
714 sediments with contrasting redox conditions, *Geochim. Cosmochim. Acta*, 74(4), 1350–1362, 2010.
- 715 Neretin, L. N., Böttcher, M. E., Jørgensen, B. B., Volkov, I. I., Lüschen, H. and Hilgenfeldt, K.: Pyritization  
716 processes and greigite formation in the advancing sulfidization front in the Upper Pleistocene sediments of the Black  
717 Sea, *Geochim. Cosmochim. Acta*, 68(9), 2081–2093, 2004.
- 718 Petzoldt, L. R.: Automatic selection of methods for solving stiff and nonstiff systems of ordinary differential  
719 equations, *SIAM J. Sci. Stat. Comput.*, 4, 136–148, 1983.
- 720 Poulton, S. and Canfield, D.: Development of a sequential extraction procedure for iron: implications for iron  
721 partitioning in continentally derived particulates, *Chem. Geol.*, 214(3-4), 209–221, 2005.
- 722 Qu, D., Ratering, S. and Schnell, S.: Microbial Reduction of Weakly Crystalline Iron (III) Oxides and Suppression of  
723 Methanogenesis in Paddy Soil, *Bull. Environ. Contam. Toxicol.*, 72(6), 1172–1181, 2004.
- 724 Raghoebarsing, A. A., Pol, A., van de Pas-Schoonen, K. T., Smolders, A. J. P., Ettwig, K. F., Rijpstra, W. I. C.,  
725 Schouten, S., Damsté, J. S. S., Op den Camp, H. J. M., Jetten, M. S. M. and Strous, M.: A microbial consortium  
726 couples anaerobic methane oxidation to denitrification, *Nature*, 440(7086), 918–921, 2006.
- 727 Rayleigh, J. W. S.: Theoretical considerations respecting the separation of gases by diffusion and similar processes,  
728 *Philos. Mag.*, (42), 493–499, 1896.
- 729 Reeburgh, W. S.: Oceanic methane biogeochemistry., *Chem. Rev.*, 107(2), 486–513, 2007.
- 730 Reed, D. C., Slomp, C. P. and Gustafsson, B. G.: Sedimentary phosphorus dynamics and the evolution of bottom-  
731 water hypoxia: A coupled benthic-pelagic model of a coastal system, *Limnol. Oceanogr.*, 56(3), 1075–1092, 2011a.
- 732 Reed, D. C., Slomp, C. P. and de Lange, G. J.: A quantitative reconstruction of organic matter and nutrient  
733 diagenesis in Mediterranean Sea sediments over the Holocene, *Geochim. Cosmochim. Acta*, 75(19), 5540–5558,  
734 2011b.
- 735 Reiche, M., Torburg, G. and Küsel, K.: Competition of Fe(III) reduction and methanogenesis in an acidic fen, *FEMS  
736 Microbiol. Ecol.*, 65(1), 88–101, 2008.



- 737 Rickard, D. and Luther, G. W.: Kinetics of pyrite formation by the H<sub>2</sub>S oxidation of iron (II) monosulfide in aqueous  
738 solutions between 25 and 125°C: The mechanism, *Geochim. Cosmochim. Acta*, 61(1), 135–147, doi:10.1016/S0016-  
739 7037(96)00322-5, 1997.
- 740 Riedinger, N., Formolo, M. J., Lyons, T. W., Henkel, S., Beck, A. and Kasten, S.: An inorganic geochemical  
741 argument for coupled anaerobic oxidation of methane and iron reduction in marine sediments, *Geobiology*, 2014.
- 742 Rooze, J., Egger, M., Tsandev, I. and Slomp, C. P.: Iron-dependent anaerobic oxidation of methane in coastal surface  
743 sediments: potential controls and impact, *Limnol. Oceanogr.*, accepted, 2016.
- 744 Ruttenberg, K. C.: Development of a sequential extraction method for different forms of phosphorus in marine  
745 sediments, *Limnol. Oceanogr.*, 37(7), 1460–1482, 1992.
- 746 Ruttenberg, K. C. and Berner, R. A.: Authigenic apatite formation and burial in sediments from non-upwelling,  
747 continental margin environments, *Geochim. Cosmochim. Acta*, 57, 991–1007, 1993.
- 748 Van Santvoort, P. J. M., De Lange, G. J., Thomson, J., Colley, S., Meysman, F. J. R. and Slomp, C. P.: Oxidation  
749 and origin of organic matter in surficial Eastern Mediterranean hemipelagic sediments, *Aquat. Geochemistry*, 8(3),  
750 153–175, 2002.
- 751 Sapart, C. J., van der Veen, C., Vigano, I., Brass, M., van de Wal, R. S. W., Bock, M., Fischer, H., Sowers, T.,  
752 Buizert, C., Sperlich, P., Blunier, T., Behrens, M., Schmitt, J., Seth, B. and Röckmann, T.: Simultaneous stable  
753 isotope analysis of methane and nitrous oxide on ice core samples, *Atmos. Meas. Tech.*, 4(12), 2607–2618, 2011.
- 754 Scheller, S., Yu, H., Chadwick, G. L., McGlynn, S. E. and Orphan, V. J.: Artificial electron acceptors decouple  
755 archaeal methane oxidation from sulfate reduction, *Science*, 351(6274), 1754–1756, 2016.
- 756 Schulz, H. D., Dahmke, A., Schinzel, U., Wallmann, K. and Zabel, M.: Early diagenetic processes, fluxes, and  
757 reaction rates in sediments of the South Atlantic, *Geochim. Cosmochim. Acta*, 58(9), 2041–2060, 1994.
- 758 Segarra, K. E. A., Comerford, C., Slaughter, J. and Joye, S. B.: Impact of electron acceptor availability on the  
759 anaerobic oxidation of methane in coastal freshwater and brackish wetland sediments, *Geochim. Cosmochim. Acta*,  
760 115, 15–30, 2013.
- 761 Seifert, R., Nauhaus, K., Blumenberg, M., Krüger, M. and Michaelis, W.: Methane dynamics in a microbial  
762 community of the Black Sea traced by stable carbon isotopes in vitro, *Org. Geochem.*, 37(10), 1411–1419, 2006.
- 763 Sivan, O., Adler, M., Pearson, A., Gelman, F., Bar-Or, I., John, S. G. and Eckert, W.: Geochemical evidence for  
764 iron-mediated anaerobic oxidation of methane, *Limnol. Oceanogr.*, 56(4), 1536–1544, 2011.
- 765 Sivan, O., Antler, G., Turchyn, A. V., Marlow, J. J. and Orphan, V. J.: Iron oxides stimulate sulfate-driven anaerobic  
766 methane oxidation in seeps, *Proc. Natl. Acad. Sci.*, 1–9, 2014.
- 767 Sivan, O., Shusta, S. and Valentine, D. L.: Methanogens rapidly transition from methane production to iron  
768 reduction, *Geobiology*, 2016.



- 769 Slomp, C. P., Epping, E. H. G., Helder, W. and Raaphorst, W. Van: A key role for iron-bound phosphorus in  
770 authigenic apatite formation in North Atlantic continental platform sediments, *J. Mar. Res.*, 54(6), 1179–1205,  
771 1996a.
- 772 Slomp, C. P., Mort, H. P., Jilbert, T., Reed, D. C., Gustafsson, B. G. and Wolthers, M.: Coupled dynamics of iron  
773 and phosphorus in sediments of an oligotrophic coastal basin and the impact of anaerobic oxidation of methane.,  
774 *PLoS One*, 8(4), e62386, 2013.
- 775 Slomp, Van der Gaast, S. J. and Van Raaphorst, W.: Phosphorus binding by poorly crystalline iron oxides in North  
776 Sea sediments, *Mar. Chem.*, 52(1), 55–73, 1996b.
- 777 Soetaert, K., Herman, P. M. J. and Middelburg, J. J.: A model of early diagenetic processes from the shelf to abyssal  
778 depths, *Geochim. Cosmochim. Acta*, 60(6), 1019–1040, 1996.
- 779 Soetaert, K. and Meysman, F.: Reactive transport in aquatic ecosystems: Rapid model prototyping in the open source  
780 software R, *Environ. Model. Softw.*, 32, 49–60, 2012.
- 781 Soetaert, K., Petzoldt, T. and Meysman, F. J. R.: marelac: Tools for Aquatic Sciences. R Package Version 2.1.3,  
782 2010.
- 783 Soulet, G., Delaygue, G., Vallet-Coulomb, C., Böttcher, M. E., Sonzogni, C., Lericolais, G. and Bard, E.: Glacial  
784 hydrologic conditions in the Black Sea reconstructed using geochemical pore water profiles, *Earth Planet. Sci. Lett.*,  
785 296(1-2), 57–66, 2010.
- 786 Soulet, G., Ménot, G., Lericolais, G. and Bard, E.: A revised calendar age for the last reconnection of the Black Sea  
787 to the global ocean, *Quat. Sci. Rev.*, 30(9-10), 1019–1026, 2011.
- 788 Strickland, J. D. and Parsons, T. R.: A Practical Handbook of Seawater Analysis, Bulletin 1., Fisheries Research  
789 Board of Canada, Ottawa, Canada., 1972.
- 790 Suess, E.: Mineral phases formed in anoxic sediments by microbial decomposition of organic matter, *Geochim.*  
791 *Cosmochim. Acta*, 43, 339–352, 1979.
- 792 Thamdrup, B., Roselló-Mora, R. and Amann, R.: Microbial manganese and sulfate reduction in Black Sea shelf  
793 sediments, *Appl. Environ. Microbiol.*, 66(2251), 2288–2297, 2000.
- 794 Treude, T., Krause, S., Maltby, J., Dale, A. W., Coffin, R. and Hamdan, L. J.: Sulfate reduction and methane  
795 oxidation activity below the sulfate-methane transition zone in Alaskan Beaufort Sea continental margin sediments:  
796 Implications for deep sulfur cycling, *Geochim. Cosmochim. Acta*, 144, 217–237, 2014.
- 797 Vargas, M., Kashefi, K., Blunt-harris, E. L. and Lovley, D. R.: Fe(III) reduction on early Earth, *Nature*, 395, 65–67,  
798 1998.
- 799 Wang, Y. and Van Cappellen, P.: A multicomponent reactive transport model of early diagenesis : Application to  
800 redox cycling in coastal marine sediments, *Geochim. Cosmochim. Acta*, 60(16), 2993–3014, 1996.



- 801 Wankel, S. D., Adams, M. M., Johnston, D. T., Hansel, C. M., Joye, S. B. and Girguis, P. R.: Anaerobic methane  
802 oxidation in metalliferous hydrothermal sediments: influence on carbon flux and decoupling from sulfate reduction,  
803 *Environ. Microbiol.*, 14(10), 2726–40, 2012.
- 804 Whiticar, M. J.: Carbon and hydrogen isotope systematics of bacterial formation and oxidation of methane, *Chem.*  
805 *Geol.*, 161(1-3), 291–314, 1999.
- 806 Yamamoto, S., Alcauskas, J. B. and Crozier, T. E.: Solubility of methane in distilled water and sea water, *J. Chem.*  
807 *Eng. Data*, 21(1), 78–80, 1976.
- 808 Yoshinaga, M. Y., Holler, T., Goldhammer, T., Wegener, G., Pohlman, J. W., Brunner, B., Kuypers, M. M. M.,  
809 Hinrichs, K. and Elvert, M.: Carbon isotope equilibration during sulphate-limited anaerobic oxidation of methane,  
810 *Nat. Geosci.*, 7, 190–194, 2014.
- 811 Zhou, S., Xu, J., Yang, G. and Zhuang, L.: Methanogenesis affected by the co-occurrence of iron(III) oxides and  
812 humic substances, *FEMS Microbiol. Ecol.*, 88(1), 107–120, 2014.
- 813 Zhuang, L., Xu, J., Tang, J. and Zhou, S.: Effect of ferrihydrite biomineralization on methanogenesis in an anaerobic  
814 incubation from paddy soil, *J. Geophys. Res. Biogeosciences*, (120), 876–886, 2015.
- 815
- 816



817 **Tables**818 **Table 1. Overview of the sequential P, Fe and S fractionation methods used in this study.**

Step and code	Extractant, extraction time	Target phase
<b>P fractionation (modified from Ruttenberg (1992); done for site 4 (MC &amp; GC) and site 5 (MC &amp; GC))</b>		
1 $P_{\text{exch}}$	1 M $MgCl_2$ , pH 8, 0.5 h	Exchangeable P
2 <sup>a</sup> $P_{\text{Fe}}$	25 g L-1 Na dithionite, pH 7.5, 8 h	Fe-associated P
3 <sup>a</sup> $P_{\text{authi Ca-P}}$	Na acetate buffer, pH 4, 6 h	P in authigenic and biogenic Ca-P minerals and $CaCO_3$
4 $P_{\text{detr}}$	1 M HCl, 24 h	Detrital P
5 $P_{\text{org}}$	Ashing at 550 °C (2h), then 1 M HCl, 24 h	Organic P
<b>Fe fractionation (after Poulton and Canfield (2005); done for site 4 (MC &amp; GC) and site 5 (MC))</b>		
1 $Fe_{\text{carb}}$	1 M Na acetate, pH 4.5, 24 h	Carbonate-associated Fe
2 $Fe_{\text{ox1}}$	1 M hydroxylamine-HCl, 24 h	Amorphous Fe oxides (ferrihydrite)
3 $Fe_{\text{ox2}}$	50 g L-1 Na dithionite, pH 4.8, 2 h	Crystalline Fe oxides (goethite, hematite)
4 $Fe_{\text{mag}}$	0.2 M ammonium oxalate/ 0.17 M oxalic acid, 2 h	Recalcitrant Fe oxides (mostly magnetite)
<b>Fe fractionation (modified from Claff et al. (2010); done for site 4 (MC &amp; GC) and site 5 (MC))</b>		
1 $Fe(II)_{\text{HCl}}$	1 M HCl, 4 h	Labile Fe (carbonates, poorly ordered sulfides)
2 $Fe(III)_{\text{HCl}}$	1 M HCl, 4 h	Labile Fe (easily reducible oxides)
3 $Fe(III)_{\text{CDB}}$	50 g L-1 Na dithionite, pH 4.8, 4 h	Crystalline Fe oxides
4 $Fe_{\text{pyrite}}$	Concentrated $HNO_3$ , 2 h	Pyrite ( $FeS_2$ )
<b>S fractionation (after Burton et al. (2008); done for site 4 (MC) and site 5 (MC &amp; GC))</b>		
1 AVS	6 M HCl, 24 h	S in Fe monosulfides ( $FeS$ )
2 CRS	Acidic chromous chloride solution, 48 h	S in pyrite ( $FeS_2$ )

819 <sup>a</sup>These steps were followed by a wash step with 1 M  $MgCl_2$ , which was added to the corresponding step. MC = multicore and GC

820 = gravity core.

821

822 **Table 2. Chemical species included in the diagenetic model.**

Species	Notation	Type
Organic matter <sup>a</sup>	$OM^{\alpha,\beta,\gamma}$	Solid
Iron oxides <sup>a</sup>	$Fe(OH)_3^{\alpha,\beta,\gamma}$	Solid
Iron monosulfide	$FeS$	Solid
Pyrite	$FeS_2$	Solid
Siderite	$FeCO_3$	Solid
Elemental sulfur	$S_0$	Solid
Iron oxide-bound phosphorus	$Fe_{ox}P$	Solid
Vivianite	$Fe_3(PO_4)_2$	Solid
Organic phosphorus	$P_{org}$	Solid
Authigenic (Ca) phosphorus	$CaP$	Solid
Detrital phosphorus	$DetrP$	Solid
Chloride	$Cl^-$	Solute
Oxygen	$O_2$	Solute
Sulfate	$SO_4^{2-}$	Solute
Iron	$Fe^{2+}$	Solute
Hydrogen sulfide <sup>b</sup>	$\Sigma H_2S$	Solute
Methane	$CH_4$	Solute
Ammonium <sup>b</sup>	$\Sigma NH_4^+$	Solute
Nitrate	$NO_3^-$	Solute
Phosphate	$\Sigma HPO_4^{2-}$	Solute
Dissolved inorganic carbon	$DIC$	Solute

823 <sup>a</sup> There are three types of species: reactive ( $\alpha$ ), less reactive ( $\beta$ ) and refractory ( $\gamma$ )824 <sup>b</sup>  $\Sigma$  denotes that all species of an acid are included

825



826 Table 3. Reaction pathways and stoichiometries implemented in the diagenetic model.

Primary redox reactions*	
$OM^{\alpha,\beta} + aO_2 \rightarrow aCO_2 + bNH_4^+ + cH_3PO_4 + aH_2O$	R1
$OM^{\alpha,\beta} + \frac{4a}{5}NO_3^- + \frac{4a}{5}H^+ \rightarrow aCO_2 + bNH_4^+ + cH_3PO_4 + \frac{2a}{5}N_2 + \frac{7a}{5}H_2O$	R2
$OM^{\alpha,\beta} + 4aFe(OH)_3^{\alpha} + 4a\chi^{\alpha}Fe_{ox}P + 12aH^+ \rightarrow aCO_2 + bNH_4^+ + (c + 4a\chi^{\alpha})H_3PO_4 + 4aFe^{2+} + 13aH_2O$	R3
$OM^{\alpha,\beta} + \frac{a}{2}SO_4^{2-} + aH^+ \rightarrow aCO_2 + bNH_4^+ + cH_3PO_4 + \frac{a}{2}H_2S + aH_2O$	R4
$OM^{\alpha,\beta} \rightarrow \frac{a}{2}CO_2 + bNH_4^+ + cH_3PO_4 + \frac{a}{2}CH_4$	R5
$CO_2 + 4H_2 \rightarrow CH_4 + 2H_2O$	R6
Secondary redox and other reaction equations†	
$2O_2 + NH_4^+ + 2HCO_3^- \rightarrow NO_3^- + 2CO_2 + 3H_2O$	R7
$O_2 + 4Fe^{2+} + 8HCO_3^- + 2H_2O + 4\chi^{\alpha}H_2PO_4^- \rightarrow 4Fe(OH)_3^{\alpha} + 4\chi^{\alpha}Fe_{ox}P + 8CO_2$	R8
$2O_2 + FeS \rightarrow SO_4^{2-} + Fe^{2+}$	R9
$7O_2 + 2FeS_2 + 2H_2O \rightarrow 4SO_4^{2-} + 2Fe^{2+} + 4H^+$	R10
$2O_2 + H_2S + 2HCO_3^- \rightarrow SO_4^{2-} + 2CO_2 + 2H_2O$	R11
$2O_2 + CH_4 \rightarrow CO_2 + 2H_2O$	R12
$2Fe(OH)_3^{\alpha} + 2\chi^{\alpha}Fe_{ox}P + H_2S + 4CO_2 \rightarrow 2Fe^{2+} + 2\chi^{\alpha}H_2PO_4^- + S_0 + 4HCO_3^- + 2H_2O$	R13
$2Fe(OH)_3^{\beta} + 2\chi^{\beta}Fe_{ox}P + H_2S + 4CO_2 \rightarrow 2Fe^{2+} + 2\chi^{\beta}H_2PO_4^- + S_0 + 4HCO_3^- + 2H_2O$	R14
$Fe^{2+} + H_2S \rightarrow FeS + 2H^+$	R15
$FeS + H_2S \rightarrow FeS_2 + H_2$	R16
$4S_0 + 4H_2O \rightarrow 3H_2S + SO_4^{2-} + 2H^+$	R17
$FeS + S_0 \rightarrow FeS_2$	R18
$SO_4^{2-} + CH_4 + CO_2 \rightarrow 2HCO_3^- + H_2S$	R19
$CH_4 + 8Fe(OH)_3^{\alpha,\beta} + 8\chi^{\alpha,\beta}Fe_{ox}P + 15H^+ \rightarrow HCO_3^- + 8Fe^{2+} + 8\chi^{\alpha,\beta}H_2PO_4^- + 21H_2O$	R20
$Fe(OH)_3^{\alpha} + (\chi^{\alpha} - \chi^{\beta})Fe_{ox}P \rightarrow Fe(OH)_3^{\beta} + (\chi^{\alpha} - \chi^{\beta})H_2PO_4^-$	R21
$Fe(OH)_3^{\beta} + (\chi^{\beta} - \chi^{\gamma})Fe_{ox}P \rightarrow Fe(OH)_3^{\gamma} + (\chi^{\beta} - \chi^{\gamma})H_2PO_4^-$	R22
$3Fe^{2+} + 2HPO_4^- \rightarrow Fe_3(PO_4)_2 + 2H^+$	R23
$Fe^{2+} + CO_3^{2-} \rightarrow FeCO_3$	R24
$FeCO_3 + H_2S \rightarrow FeS + HCO_3^- + H^+$	R25
$Fe_3(PO_4)_2 + 3H_2S \rightarrow 3FeS + 2HPO_4^{2-} + 4H^+$	R26

827 \* Organic matter (OM) is of the form  $(CH_2O)_a(NH_4^+)_b(H_3PO_4)_c$ , with 'a'=1, 'b' = 1/16 and 'c' = 1/106. Under anoxic bottom828 water conditions, 'c' reduces to 0.25. †  $\chi^{\alpha,\beta,\gamma}$  refers to the P:Fe ratio of  $Fe(OH)_3^{\alpha,\beta,\gamma}$  (see Supplementary Table S1). R6 = CO<sub>2</sub>829 reduction; R7 = nitrification; R8 = Fe(OH)<sub>3</sub> formation; R9 = FeS oxidation; R10 = FeS<sub>2</sub> oxidation; R11 = H<sub>2</sub>S oxidation; R12 =830 aerobic CH<sub>4</sub> oxidation; R13 and R14 = Fe(OH)<sub>3</sub> reduction by H<sub>2</sub>S; R15 = FeS formation; R16 = pyrite formation (H<sub>2</sub>S pathway);831 R17 = S<sub>0</sub> disproportionation; R18 = pyrite formation (polysulfide pathway); R19 = SO<sub>4</sub>-AOM; R20 = Fe-AOM; R21 = conversion

832 (i.e. crystallization) from α to β phase; R22 = crystallization from β to γ phase; R23 = vivianite formation; R24 = siderite

833 precipitation; R25 = conversion from siderite to FeS; R26 = vivianite dissolution by dissolved sulfide

834

835



836

837 **Table 4. Reaction equations implemented in the model.**

Primary redox reaction equations	
$R_1 = k_{\alpha,\beta} OM^{\alpha,\beta} \left( \frac{[O_2]}{K_{O_2} + [O_2]} \right)$	(E1)
$R_2 = k_{\alpha,\beta} OM^{\alpha,\beta} \left( \frac{[NO_3^-]}{K_{NO_3^-} + [NO_3^-]} \right) \left( \frac{K_{O_2}}{K_{O_2} + [O_2]} \right)$	(E2)
$R_3 = k_{\alpha,\beta} OM^{\alpha,\beta} \left( \frac{[Fe(OH)_3^{\alpha}]}{K_{Fe(OH)_3^{\alpha}} + [Fe(OH)_3^{\alpha}]} \right) \left( \frac{K_{NO_3^-}}{K_{NO_3^-} + [NO_3^-]} \right) \left( \frac{K_{O_2}}{K_{O_2} + [O_2]} \right)$	(E3)
$R_4 = \Psi k_{\alpha,\beta} OM^{\alpha,\beta} \left( \frac{[SO_4^{2-}]}{K_{SO_4^{2-}} + [SO_4^{2-}]} \right) \left( \frac{K_{Fe(OH)_3^{\alpha}}}{K_{Fe(OH)_3^{\alpha}} + [Fe(OH)_3^{\alpha}]} \right) \left( \frac{K_{NO_3^-}}{K_{NO_3^-} + [NO_3^-]} \right) \left( \frac{K_{O_2}}{K_{O_2} + [O_2]} \right)$	(E4)
$R_5 = \Psi k_{\alpha,\beta} OM^{\alpha,\beta} \left( \frac{K_{SO_4^{2-}}}{K_{SO_4^{2-}} + [SO_4^{2-}]} \right) \left( \frac{K_{Fe(OH)_3^{\alpha}}}{K_{Fe(OH)_3^{\alpha}} + [Fe(OH)_3^{\alpha}]} \right) \left( \frac{K_{NO_3^-}}{K_{NO_3^-} + [NO_3^-]} \right) \left( \frac{K_{O_2}}{K_{O_2} + [O_2]} \right)$	(E5)
$R_6 = k_1 DIC \left( \frac{K_{SO_4^{2-}}}{K_{SO_4^{2-}} + [SO_4^{2-}]} \right) \left( \frac{K_{Fe(OH)_3^{\alpha}}}{K_{Fe(OH)_3^{\alpha}} + [Fe(OH)_3^{\alpha}]} \right) \left( \frac{K_{NO_3^-}}{K_{NO_3^-} + [NO_3^-]} \right) \left( \frac{K_{O_2}}{K_{O_2} + [O_2]} \right)$	(E6)
Secondary redox and other reaction equations	
$R_7 = k_2 [O_2] [NH_4^+]$	(E7)
$R_8 = k_3 [O_2] [Fe^{2+}]$	(E8)
$R_9 = k_4 [O_2] [FeS]$	(E9)
$R_{10} = k_5 [O_2] [FeS_2]$	(E10)
$R_{11} = k_6 [O_2] [\Sigma H_2S]$	(E11)
$R_{12} = k_7 [O_2] [CH_4]$	(E12)
$R_{13} = k_8 [Fe(OH)_3^{\alpha}] [\Sigma H_2S]$	(E13)
$R_{14} = k_9 [Fe(OH)_3^{\beta}] [\Sigma H_2S]$	(E14)
$R_{15} = k_{10} [Fe^{2+}] [\Sigma H_2S]$	(E15)
$R_{16} = k_{11} [FeS] [\Sigma H_2S]$	(E16)
$R_{17} = k_{12} [S_0]$	(E17)
$R_{18} = k_{13} [FeS] [S_0]$	(E18)
$R_{19} = k_{14} [SO_4^{2-}] [CH_4]$	(E19)
$R_{20} = k_{15} [Fe(OH)_3^{\alpha,\beta}] [CH_4]$	(E20)
$R_{21} = k_{16} [Fe(OH)_3^{\alpha}]$	(E21)
$R_{22} = k_{17} [Fe(OH)_3^{\beta}]$	(E22)
$R_{23} = k_{18} [Fe^{2+}] [HPO_4^{2-}]$	(E23)
$R_{24} = k_{19} [Fe^{2+}] [DIC]$	(E24)
$R_{25} = k_{20} [FeCO_3] [\Sigma H_2S]$	(E25)
$R_{26} = k_{21} [Fe_3(PO_4)_2] [\Sigma H_2S]$	(E26)

838

839

840 **Table 5. Reaction parameters used in the diagenetic model.**

Parameter	Symbol	Value	Units	Values given in literature
Decay constant for $C_{org}^{\alpha}$	$k_{\alpha}$	0.05	yr <sup>-1</sup>	0.05-1.62 <sup>a,b</sup>
Decay constant for $C_{org}^{\beta}$	$k_{\beta}$	0.0086	yr <sup>-1</sup>	0.0086 <sup>b</sup>
Limiting concentration of O <sub>2</sub>	$K_{O_2}$	0.02	mM	0.001-0.03 <sup>c</sup>
Limiting concentration of NO <sub>3</sub> <sup>-</sup>	$K_{NO_3^-}$	0.004	mM	0.004-0.08 <sup>c</sup>
Limiting concentration of Fe(OH) <sub>3</sub>	$K_{Fe(OH)_3}$	65	μmol g <sup>-1</sup>	65-100 <sup>c</sup>
Limiting concentration of SO <sub>4</sub> <sup>2-</sup>	$K_{SO_4^{2-}}$	1.6	mM	1.6 <sup>c</sup>
Attenuation factor for SO <sub>4</sub> <sup>2-</sup> and methanogenesis	$\Psi$	0.0042	-	0.00157-0.075 <sup>b,d</sup>
Rate constant for reaction <i>E6</i>	$k_1$	0.0011	yr <sup>-1</sup>	
Rate constant for reaction <i>E7</i>	$k_2$	10 <sup>3</sup> 000	mM <sup>-1</sup> yr <sup>-1</sup>	5 <sup>3</sup> 000-39 <sup>3</sup> 000 <sup>c,d</sup>
Rate constant for reaction <i>E8</i>	$k_3$	140 <sup>3</sup> 000	mM <sup>-1</sup> yr <sup>-1</sup>	140 <sup>3</sup> 000 <sup>c</sup>
Rate constant for reaction <i>E9</i>	$k_4$	300	mM <sup>-1</sup> yr <sup>-1</sup>	300 <sup>c</sup>
Rate constant for reaction <i>E10</i>	$k_5$	1	mM <sup>-1</sup> yr <sup>-1</sup>	1 <sup>c</sup>
Rate constant for reaction <i>E11</i>	$k_6$	160	mM <sup>-1</sup> yr <sup>-1</sup>	≥ 160 <sup>c</sup>
Rate constant for reaction <i>E12</i>	$k_7$	10 <sup>3</sup> 000 <sup>3</sup> 000	mM <sup>-1</sup> yr <sup>-1</sup>	10 <sup>3</sup> 000 <sup>3</sup> 000 <sup>c</sup>
Rate constant for reaction <i>E13</i>	$k_8$	9.5	mM <sup>-1</sup> yr <sup>-1</sup>	≤ 100 <sup>c</sup>
Rate constant for reaction <i>E14</i>	$k_9$	0.95	mM <sup>-1</sup> yr <sup>-1</sup>	Model constrained
Rate constant for reaction <i>E15</i>	$k_{10}$	150	mM <sup>-1</sup> yr <sup>-1</sup>	100-14 <sup>3</sup> 800 <sup>b,d</sup>
Rate constant for reaction <i>E16</i>	$k_{11}$	0.0003	mM <sup>-1</sup> yr <sup>-1</sup>	3.15 <sup>c</sup>
Rate constant for reaction <i>E17</i>	$k_{12}$	3	yr <sup>-1</sup>	3 <sup>f</sup>
Rate constant for reaction <i>E18</i>	$k_{13}$	1	mM <sup>-1</sup> yr <sup>-1</sup>	7 <sup>f</sup>
Rate constant for reaction <i>E19</i>	$k_{14}$	0.14	mM <sup>-1</sup> yr <sup>-1</sup>	10 <sup>c</sup>
Rate constant for reaction <i>E20</i>	$k_{15}$	0.00000016	mM <sup>-1</sup> yr <sup>-1</sup>	0.0074 <sup>g</sup>
Rate constant for reaction <i>E21</i>	$k_{16}$	0.6	yr <sup>-1</sup>	0.6 <sup>f</sup>
Rate constant for reaction <i>E22</i>	$k_{17}$	0.000013	yr <sup>-1</sup>	Model constrained
Rate constant for reaction <i>E23</i>	$k_{18}$	0.052	mM <sup>-1</sup> yr <sup>-1</sup>	Model constrained
Rate constant for reaction <i>E24</i>	$k_{19}$	0.0027	mM <sup>-1</sup> yr <sup>-1</sup>	Model constrained
Rate constant for reaction <i>E25</i>	$k_{20}$	0.0008	mM <sup>-1</sup> yr <sup>-1</sup>	Model constrained
Rate constant for reaction <i>E26</i>	$k_{21}$	0.0008	mM <sup>-1</sup> yr <sup>-1</sup>	Model constrained

841 <sup>a</sup> Moodley et al. (2005); <sup>b</sup> Reed et al. (2011a); <sup>c</sup> Wang and Van Cappellen (1996); <sup>d</sup> Reed et al. (2011b); <sup>e</sup> Rickard and Luther842 (1997); <sup>f</sup> Berg et al. (2003); <sup>g</sup> Rooze et al. (2016)

843

844

845

846 **Table 6. Depth-integrated rates of key processes for selected depth intervals in  $\mu\text{mol m}^{-2} \text{d}^{-1}$ .**

Process	0 – 90 cm <sup>a</sup>	90 - 300 cm <sup>b</sup>	300 – 800 cm <sup>c</sup>	0 – 800 cm
Organoclastic $\text{SO}_4^{2-}$ reduction	698.12	22.20	0.012	720.34
Methanogenesis (OM)	18.81	12.02	46.24	77.07
Methanogenesis (DIC)	0.35	17.24	40.33	57.92
$\text{SO}_4$ - AOM	10.05	157.42	1.37	168.83
Fe – AOM <sup>d</sup>	0	0	0.14	0.14
$\text{S}_0$ disproportionation	0	0	1.13	1.13

847 <sup>a</sup> Marine deposits ; <sup>b</sup> limnic sediments around the SMTZ with dissolved sulfide; <sup>c</sup> non-sulfidic limnic deposits; <sup>d</sup> per mol of  $\text{CH}_4$ 

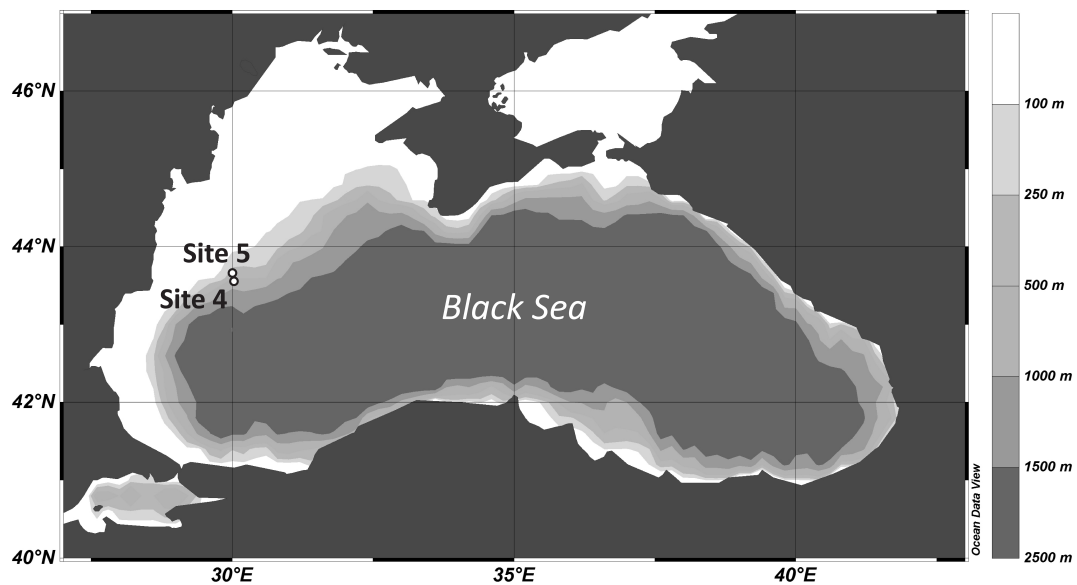
848

849

850



851 **Figures**

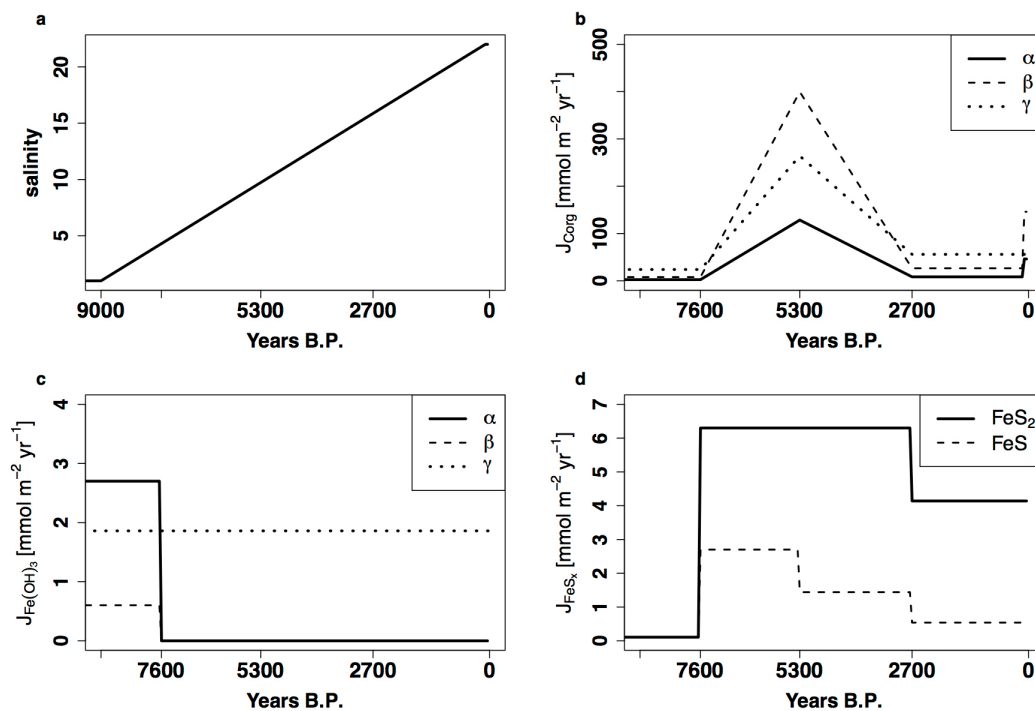


852

853 **Figure 1.** Map showing the locations of site 4 (43°40.6' N, 30°7.5' E; 377 mbss) and site 5 (43°42.6' N, 30°6.1' E; 178 mbss),  
854 sampled in June 2013.

855

856



857

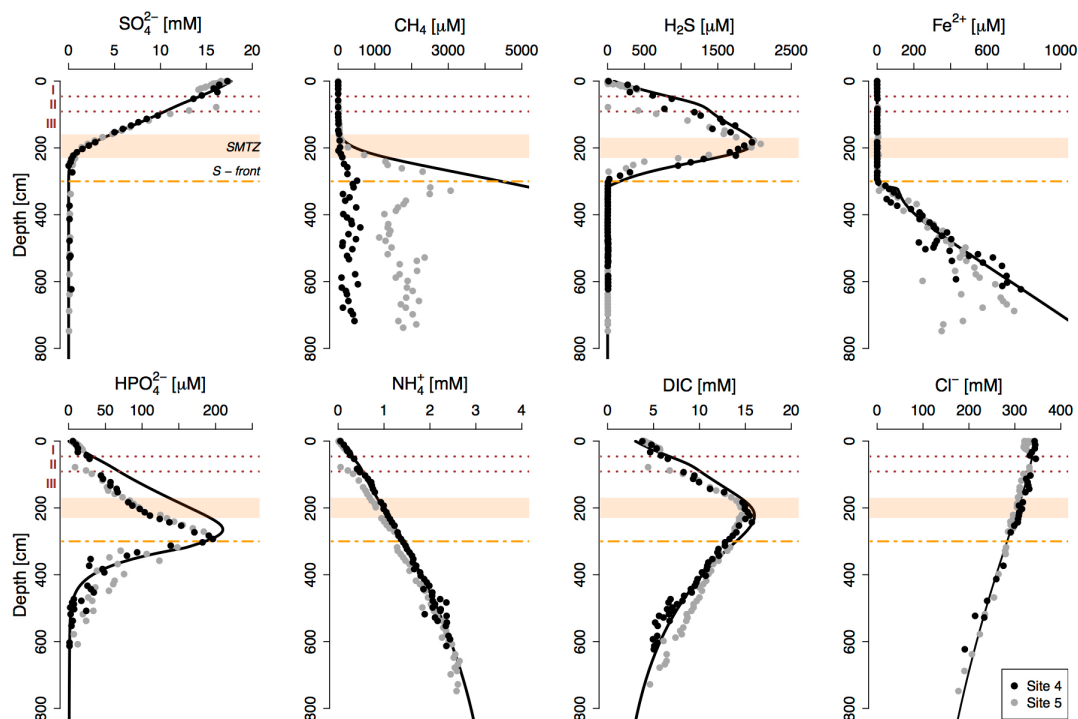
858

859

Figure 2. Transient evolution of salinity with a linear increase from 1 to 22 between 9000 and 100 years B.P. (a), fluxes of organic matter ( $J_{C_{org}}$ ; b), Fe oxides ( $J_{Fe(OH)_3}$ ; c) and Fe sulfides ( $J_{FeS_x}$ ; d) as implemented in the diagenetic model (site 4).

860



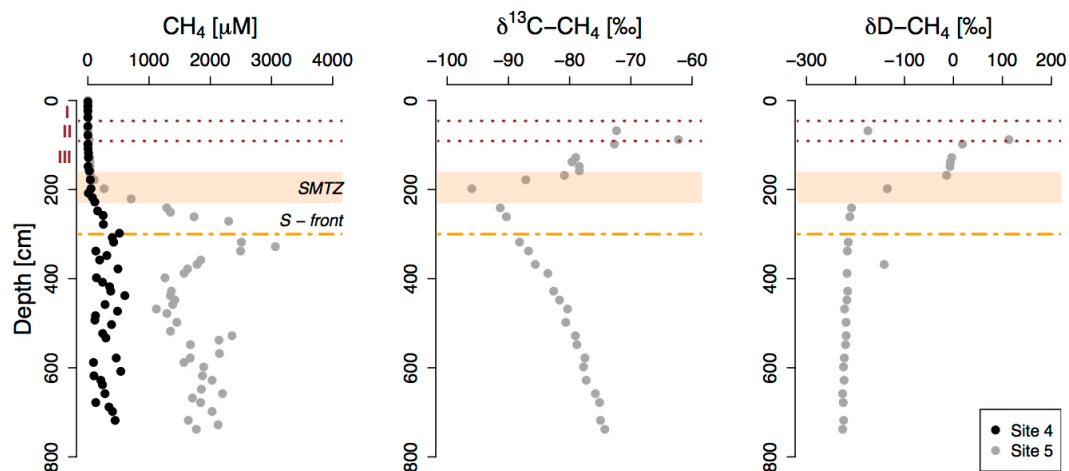


861

862 **Figure 3.** Pore water profiles of key components for site 4 (black dots) and site 5 (gray dots) and corresponding modeled  
 863 profiles as calculated with the diagenetic model (black lines). Red dotted lines and roman numbers indicate the transitions  
 864 between the lithological Unit I (modern coccolith ooze), Unit II (marine sapropel) and Unit III (limnic deposits). The  
 865 orange bar represents the sulfate-methane transition zone (SMTZ) and the orange dashed line shows the current position  
 866 of the downward migrating sulfidization front (S-front).

867

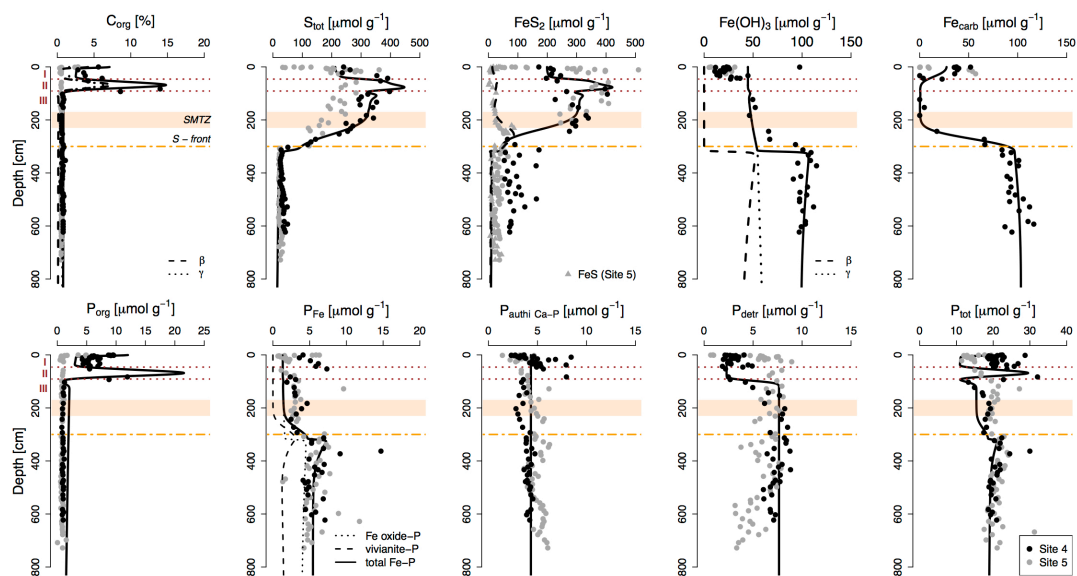
868



869

870 Figure 4. Pore water profiles of  $\text{CH}_4$  for site 4 (black dots) and 5 (gray dots) and corresponding isotopic composition of  
871 dissolved  $\text{CH}_4$  (available for site 5 only).  $\delta^{13}\text{C}-\text{CH}_4$  values are given in ‰ vs. VPDB (Vienna Pee Dee Belemnite) and  $\delta\text{D}-$   
872  $\text{CH}_4$  values are given in ‰ vs. V-SMOW (Vienna Standard Mean Ocean Water). Red dotted lines and roman numbers  
873 indicate the transitions between the lithological Unit I (modern coccolith ooze), Unit II (marine sapropel) and Unit III  
874 (limnic deposits). The orange bar represents the sulfate-methane transition zone (SMTZ) and the orange dashed line  
875 shows the current position of the downward migrating sulfidization front (S-front).

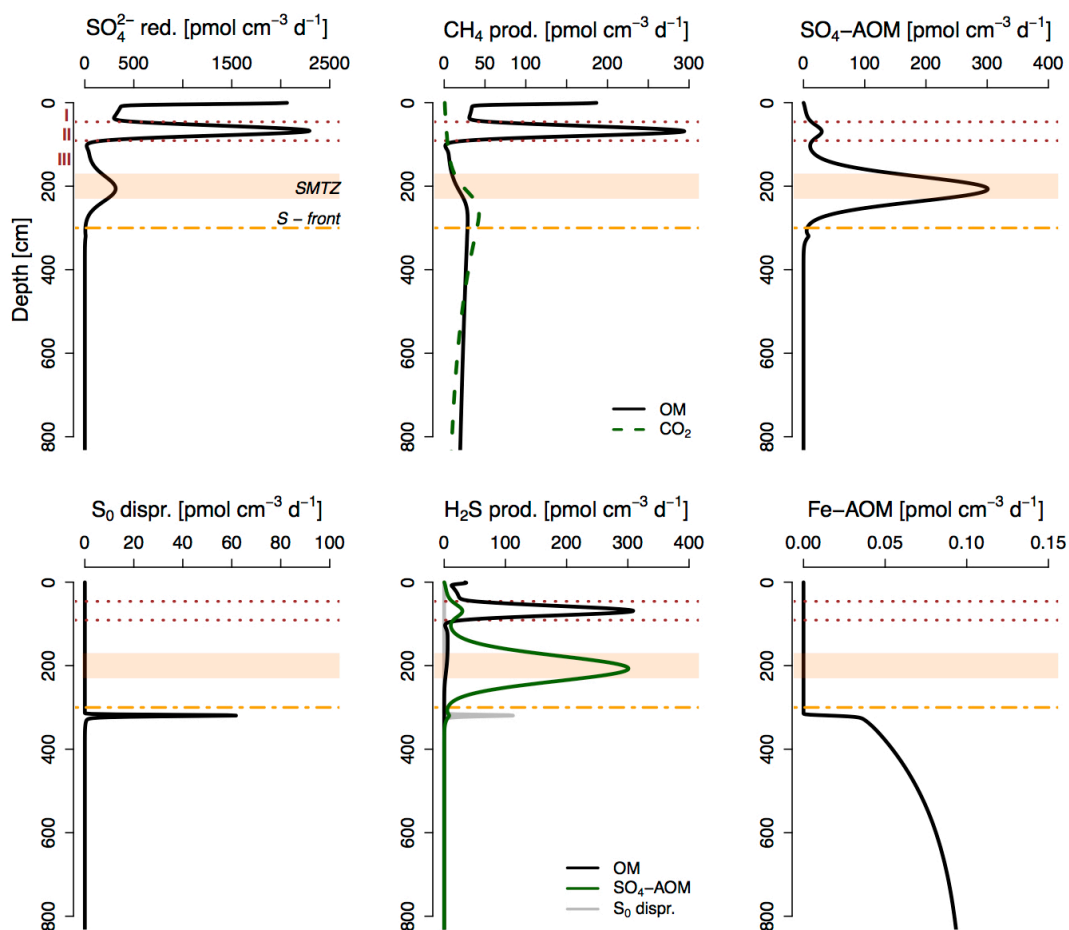
876



877

878 **Figure 5.** Solid phase sediment profiles for site 4 (black dots) and 5 (gray dots). Fe oxides represent the sum of amorphous,  
 879 crystalline and recalcitrant oxides, i.e.  $Fe_{ox1}$ ,  $Fe_{ox2}$  and  $Fe_{mag}$  (Table 1, Supplementary Fig. S2).  $Fe_{carb}$  was corrected for  
 880 apparent AVS dissolution during the Na acetate extraction step (the uncorrected  $Fe_{carb}$  data is given in Supplementary  
 881 Fig. S2). Black lines represent profiles derived from the diagenetic model. Red dotted lines and roman numbers indicate  
 882 the transitions between the lithological Unit I (modern coccolith ooze), Unit II (marine sapropel) and Unit III (limnic  
 883 deposits). The orange bar represents the sulfate-methane transition zone (SMTZ) and the orange dashed line shows the  
 884 current position of the downward migrating sulfidization front (S-front).

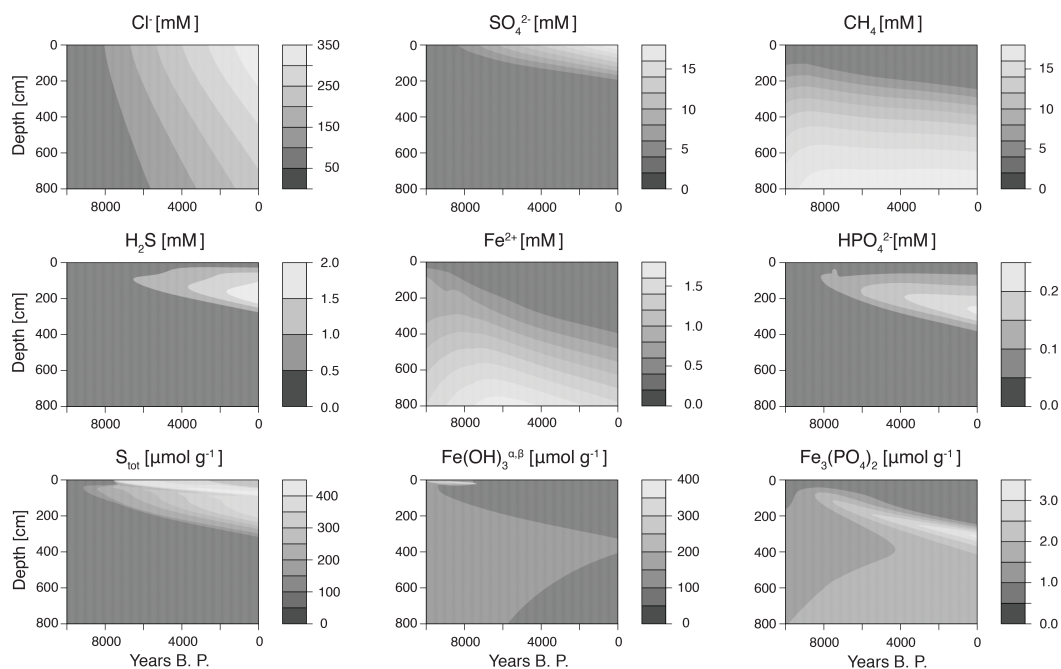
885



886

887 **Figure 6.** Modeled rates of total  $\text{SO}_4^{2-}$  reduction, methanogenesis,  $\text{SO}_4$ -AOM,  $\text{S}_0$  disproportionation, sulfide production  
 888 and Fe-AOM. Methanogenesis is divided into  $\text{CH}_4$  production from organic matter fermentation (“OM”; black solid line)  
 889 and  $\text{CO}_2$  reduction (“ $\text{CO}_2$ ”; green dashed line). Red dotted lines and roman numbers indicate the transitions between the  
 890 lithological Unit I (modern coccolith ooze), Unit II (marine sapropel) and Unit III (limnic deposits). The orange bar  
 891 represents the sulfate-methane transition zone (SMTZ) and the orange dashed line shows the current position of the  
 892 downward migrating sulfidization front (S-front).

893



894

895

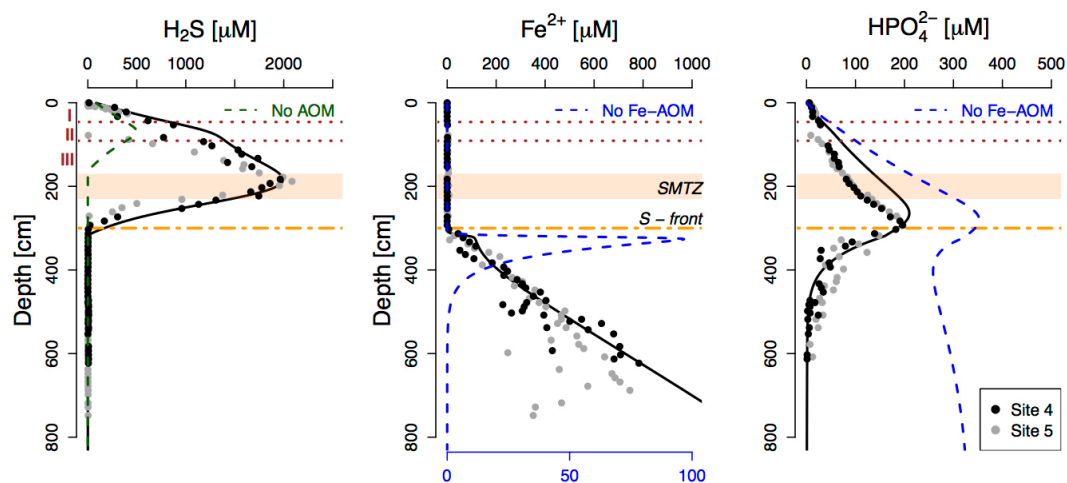
**Figure 7. Transient evolution of selected pore water and sediment profiles with depth as calculated for site 4 using the diagenetic model.**

896

897



898



899

900

901

902

903

904

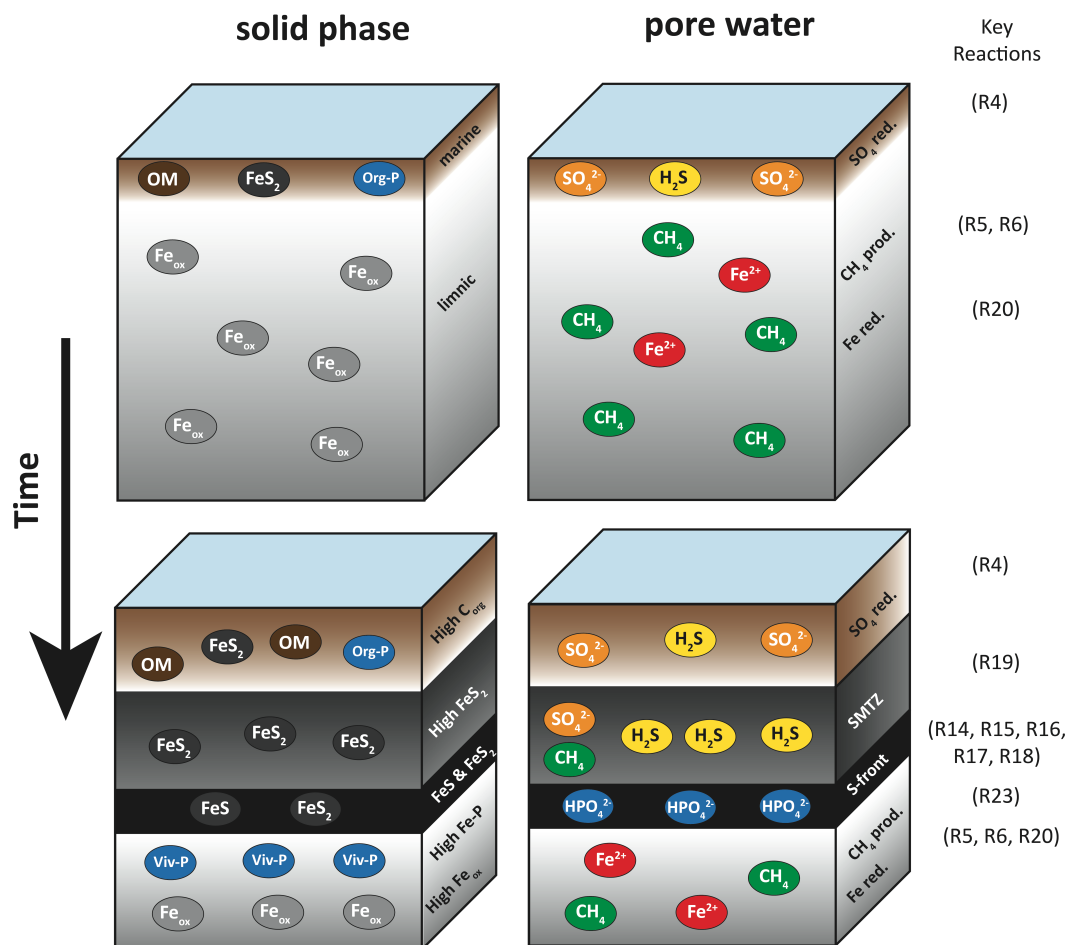
905

906

907

908

Figure 8. Pore water profiles of dissolved sulfide,  $\text{Fe}^{2+}$  and  $\text{HPO}_4^{2-}$ . The green dashed line represents the modeled sulfide profile without  $\text{SO}_4$ -AOM, indicating that latter significantly enhances the downward sulfidization. Blue dashed lines denote the modeled  $\text{Fe}^{2+}$  and  $\text{HPO}_4^{2-}$  profiles without ongoing Fe oxide reduction in the limnic deposits (i.e. no Fe-AOM). Note that concentrations of  $\text{Fe}^{2+}$  were multiplied 10 times in the model simulation without Fe oxide reduction to better visualize the potential release of  $\text{Fe}^{2+}$  through a cryptic S cycle (corresponding x axis at bottom). Red dotted lines and roman numerals indicate the transitions between the lithological Unit I (modern coccolith ooze), Unit II (marine sapropel) and Unit III (limnic deposits). The orange bar represents the sulfate-methane transition zone (SMTZ) and the orange dashed line shows the current position of the downward migrating sulfidization front (S-front).



909

910 **Figure 9.** Schematic of the main diagenetic processes discussed in this study and their imprint on the geochemical solid  
 911 phase (left) and pore water profiles (right). Accumulation of marine sediments with time and the subsequent downward  
 912 diffusion of SO<sub>4</sub><sup>2-</sup> into the CH<sub>4</sub>-bearing limnic sediment stimulate SO<sub>4</sub>-AOM around the sulfate-methane transition zone  
 913 (SMTZ), thus enhancing the downward sulfidization of the Fe oxide-rich lake deposits. Below the sulfidization front (S-  
 914 front), HPO<sub>4</sub><sup>2-</sup> released during reductive dissolution of Fe oxides is bound again in vivianite, leading to an enrichment in  
 915 sedimentary P in these sediments. Numbers on the right indicate the key reactions occurring in the corresponding  
 916 sediment layers as described in Table 3. Note that in this study, Fe-AOM (R20) represents the main source of pore water  
 917 Fe<sup>2+</sup> below the S-front. However, based on the geochemical data, we cannot exclude a potential role for organoclastic Fe  
 918 reduction (R3).